UC Riverside

UC Riverside Electronic Theses and Dissertations

Title

High Density Three-Dimensional Nanomagnetic Logic Systems Composed of Material with Crystalline Anisotropy

Permalink

https://escholarship.org/uc/item/934551tc

Author

Tian, Yuan

Publication Date

2013

Peer reviewed|Thesis/dissertation

eScholarship.org Powered by the California Digital Library
University of California

UNIVERSITY OF CALIFORNIA
RIVERSIDE

High Density Three-Dimensional Nanomagnetic Logic Systems Composed of Material with Crystalline Anisotropy

A Dissertation submitted in partial satisfaction
of the requirements for the degree of

Doctor of Philosophy

in

Electrical Engineering

by

Yuan Tian

June 2013

Dissertation Committee:
Dr. Ilya Dumer, Chairperson
Dr. Sakhrat Khizroev
Dr. Ping Liang

Copyright by
Yuan Tian
2013

The Dissertation of Yuan Tian is approved:

_____

_____

_____

Committee Chairperson

University of California, Riverside

ACKNOWLEDGMENTS

First and foremost, I would like to express my gratitude to Prof. Sakhrat Khizroev and Prof. Ilya Dumer for being my advisors. During the past five years, their guidance and support made me successful in my doctoral research. Meanwhile, I truly appreciate Prof. Ping Liang for his valuable advice.

Thank all my colleagues at the Center for 3D Electronics at UCR (listed in alphabetical order of their first names): Alexander (Sasha) Krichevsky, Andrey Lavrenov, Beomseop Lee, Bing Hu, Chen Zhang, Jeongmin Hong, Matthew Hudgins, Nissim Amos, Rabee Ikkawi, Robert Fernandez, and Steven Chen. Special thanks to Nissim for all his kind and patient help with my research.

Thank UCR College Chancellor's Fellowship, National Science Foundation (NSF), Department of Defense (DoD), and Defense MicroElectronics Activity (DMEA) for providing financial support.

I dedicate all my work to my parents, Xin Cai and Gang Tian, for their love, endless support and encouragement.

ABSTRACT OF THE DISSERTATION

High Density Three-Dimensional Nanomagnetic Logic Systems Composed of Material with Crystalline Anisotropy

by

Yuan Tian

Doctor of Philosophy, Graduate Program in Electrical Engineering
University of California, Riverside, June 2013
Dr. Ilya Dumer, Chairperson

In the past decades, semiconductor industry has been enhancing the performance of silicon-based processor through downsizing the size of transistors. However, miniaturization is approaching the physical limits. Difficulties like floating gate interference, low coupling ratio, and heat dissipation are increasingly severe. Therefore, nanoscale magnetic logic system, as a prominent alternative technology, is being studied.

A theoretical study is reported to use a patterned network of nanomagnets (nanocells) as a new architecture for next-generation computing processors, in which the direction of the magnetization represents a binary signal in each cell.

Such shape-insensitive nanomagnetic devices can relieve severe fabrication constraints associated with building nanomagnetic cells of narrowly defined shapes. Particularly, comparison between materials with in-plane and out-of-plane crystalline anisotropy is presented. Properties of materials with in-plane crystalline anisotropy can be tailored to match those of shape-induced longitudinal nanomagnets while materials with out-of-plane anisotropy could enable a new set of features. For instance, besides the key features

of any magnetic logic, i.e., non-volatility, low-power consumption, and radiation hardness, some of the new features of the out-of-plane materials include (i) cost-effective fabrication, (ii) scalability to sub-10-nm dimensions, and (iii) their natural ability to be extended into a three-dimensional (3-D) physical space which opens a new era of technology opportunities.

Implementation of a high density three-layer magnetic recording device is introduced. It proves the feasibility of using multilayer nanomagnetic material with perpendicular anisotropy to store 2^N levels of signal (N is the amount of magnetic layers). Related experimental results are demonstrated. Moreover, similar three-dimensional four-layer architecture is proven to be a potential candidate of building majority logic gates.

Development of energy-efficient spin-transfer torque (STT) magnetization reversal in sub-10nm magnetic tunneling junction (MTJ) point contacts is also explored. Reducing required switching current of STT-MTJ is an essential and practical issue in the manufacturing industry of STT-based MRAM. Both simulation and experimental results show the switching current requirement is at least an order magnitude less in devices of length in sub-10nm region, which has great importance for developing next generation MRAM. Besides, experimental results show there is little relevance between contact resistance and the TMR effect amplitude.

Table of Contents

List of Figures

List of Tables

Chapter 1 Research Motivation

Silicon-based semiconductor manufacturing industry has met severe difficulties in enhancing processor performance by continuously shrinking the size of transistor. Thermal noise and cross-talk seem to be inevitable and prevents increasing the area density of silicon transistor in chip. Magnetic logic system, benefited from its extremely low power consumption and the non-volatile feature, provides an alternative way to the new ear of computing and information storage.

Limitations of Conventional Technologies

Moore's Law [1], which originated from Gordon Moore's observation over the development of integrated chips in the 1960s, represents the trend of the rapid growth of semiconductor industry in the past 50 years. The law says that the number of transistor in the same area of silicon substrate will be doubled every 24 months. However, after being in rule for almost half a century, Moore's Law has finally stumbled on various fundamental limits [2,3]. Degrading effects such as severe floating gate interference, a low coupling ratio, short channel effects, low electron charge in the floating gate, and many others, are starting to literally multiply and thus eventually putting an end to the traditional advancement through scaling of CMOS technologies [4] (Figure 1). It is hard to see how the industry will be able to further shrink a node size below 10 nm which is equivalent to a square information cell size of barely reaching approximately 20 nm on a side [5,6].

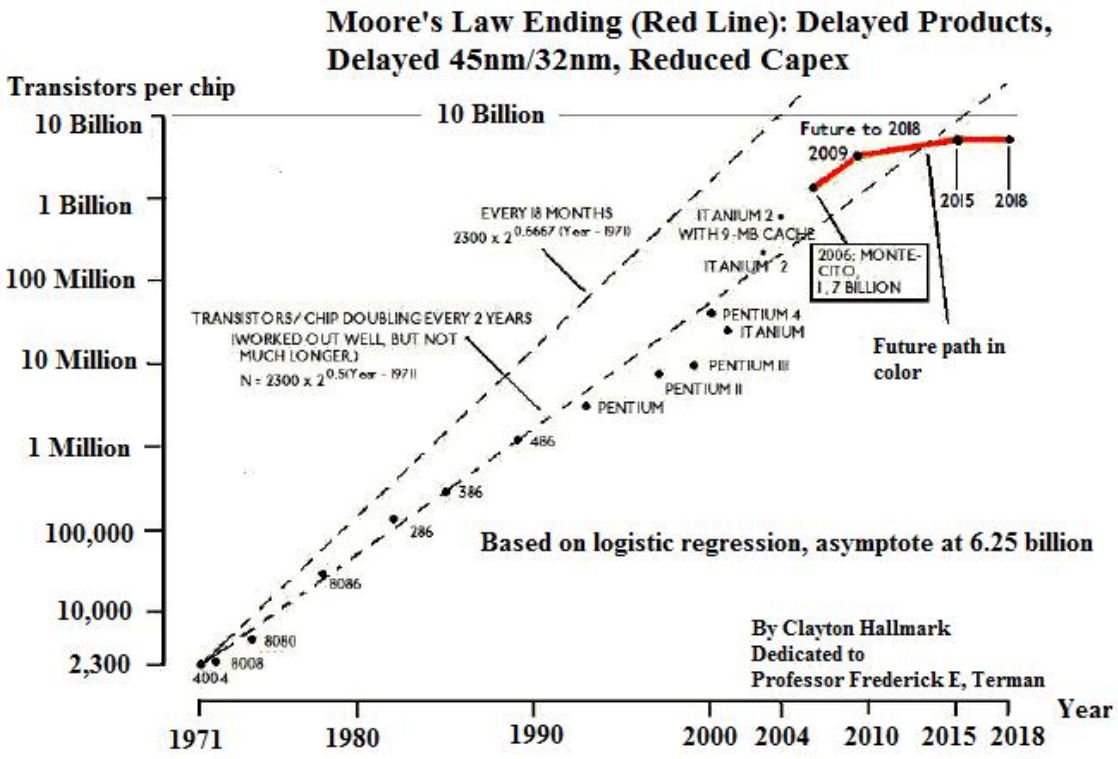

Figure 1: Moore's Law Ending [7]. The clock speed increased much slower after 2003, while transistor count still doubled every 24 month due to the enlargement of chip area.

According to the 2010 update to the International Technology Roadmap for Semiconductors (ITRS) [8], devices based on silicon-only technology will grow much slower after 2013. The transistor densities will only be double no less than every three years. Nowadays, although the transistor count is still increasing, the chip area is enlarged significantly at the same moment. The competition of clocking frequency has been replaced by competition of multi-cores. Chip designers and manufacturers are looking for new materials and techniques can start a new era. It is not surprising why over the past few years all the main advancements in the industry occurred through optimization of

materials and device configurations, especially through increasing the cores in a chip, rather than through radical scaling as it did in the past [9].

On the contrary, magnetic logic technologies promise scalability down to a sub-10-nanometer bit size [10]. The current downfall of silicon technologies might be a turning point and a great opportunity for magnetic counterparts to finally exploit their technical superiority. Besides radiation hardness and non-volatility, the other projected key advantages of magnetic devices include low-power consumption – with orders of magnitude improvement compared to silicon technologies, and great scalability – with potential packing density a few orders of magnitude superior to that of today's transistor based logic.

In addition, arguably the problem of cascading, especially AC fan-out, is not as severe in magnetic logic as it is in CMOS technologies and therefore ideally magnetic logic systems can provide more flexibility in the design. Also, magnetic logic can be naturally integrated with the well-established magnetic storage technology to emerge into a single-chip computing paradigm. Finally, unlike the charge in semiconductor devices, the magnetic moment can be partially polarized. Three-dimensional (3D) architectures (with partially polarized states) come natural to magnetic devices and therefore magnetic logic may pave a way for the industry to step into the emerging era of three-dimensional technology dynasty [11].

Overview of Magnetic Logic Systems

Magnetic computing technologies were competing with their semiconductor counterparts from the emergence of modern computing hardware concepts about a century ago [12,13]. Their well-known advantages are radiation hardness and non-volatility [14]. Nevertheless, with the emergence of semiconductor integrated circuits in early 60s, the cost-driven computer industry was forced to abandon magnetic solutions in favor of cost-effective and scalable silicon technologies.

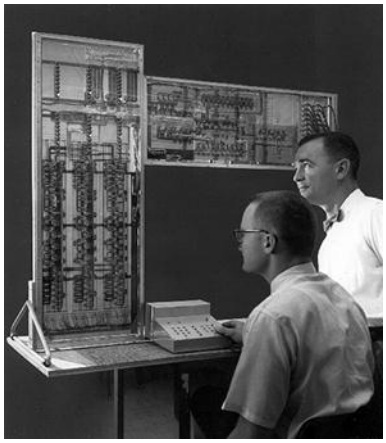

Figure 2: An all-magnetic computer built in 1961 by the SRI magnetics group funded by U.S. Air Force [15].

In the past decade, the opportunity to realize non-volatile logic functions with novel nanomagnetic structures has attracted great attention especially in the academic community [16]. The rapidly emerging magnetic computing might become one of the most promising technologies to overcome scaling limitations of silicon-based processors and therefore enable many future generations of computing and storage technologies.

Magnetic Quantum-dot Cellular Automata (MQCA)

One of the most popular magnetic logic architectures relies on exploiting a patterned network of nanomagnets (PNON), widely known as a Magnetic Quantum-dot Cellular Automata (MQCA) [17,18]. In this configuration, magnetic materials are fabricated into nanomagnets (cells) that have single domain features. The magnetic coupling between adjacent cells, including both magnetostatic and quantum-mechanical exchange contributions, can be controlled to (i) change their respective magnetization directions as well as (ii) define magnetic states in pre-selected output cells. Therefore, by learning to control the coupling, it is possible to accomplish the two main functions of computing, i.e. (i) to transmit a binary signal within a circuit from point A to point B and (ii) to perform a basic set of logic operations in which an output signal (in the output cell(s)) depends on several input signals (in the input cells). Further throughout the text, to be consistent with conventional terminology, the two functions will be referred to be as data channels and majority logic gates, respectively.

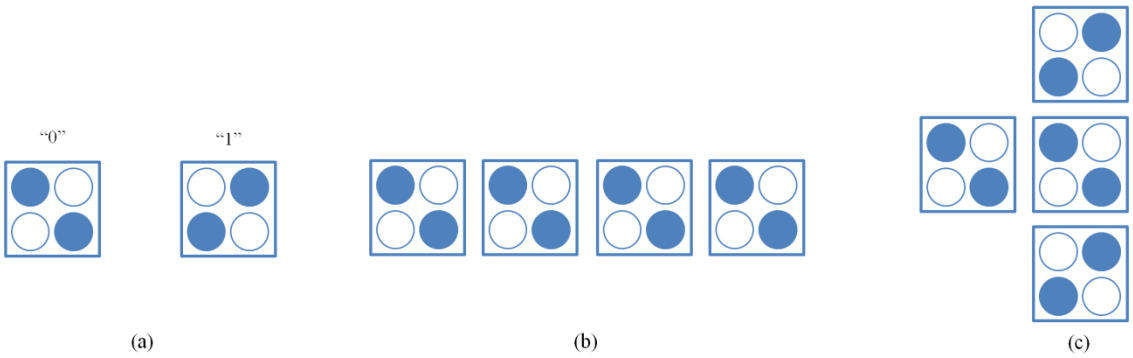

Figure 3: (a) Bistable quantum-dot automata units denoting "0" and "1"; (b) Binary QCA wire (data channel); (c) A QCA majority gates

Figure 3 shows the semantics of quantum-dot cellular automata (QCA), which is a computational abstract paradigm that can be implemented with bistable units having

field-coupling effect [19,20]. After assembling these units into arrays, binary signal propagation (data channel, Figure 3b) and logic functions (Figure 3c) can be implemented. Due to larger energy barrier between bistable states, a great advantage of magnetic QCA system over its electronic sibling is that MQCA can operates under room temperature, instead of environments of extremely low temperature.

Previous research on MQCA focused on using mostly soft materials, such as Permalloy, to fabricate nanomagnetic cells. Using soft materials implies that the anisotropy of each nanomagnet is defined by its shape. Various researchers have already shown that Permalloy nanocells indeed can have adequate bi-stability, ferromagnetic (FC) and antiferromagnetic (AFC) coupling interactions, which are the most crucial features necessary for both of the propagation of binary signals [21,22]and the implementation of logic gates. The physics of the energy barrier between the ground state and metastable states of two coupled nanomagnets was also extensively discussed in literature [23,24] (Figure 4).

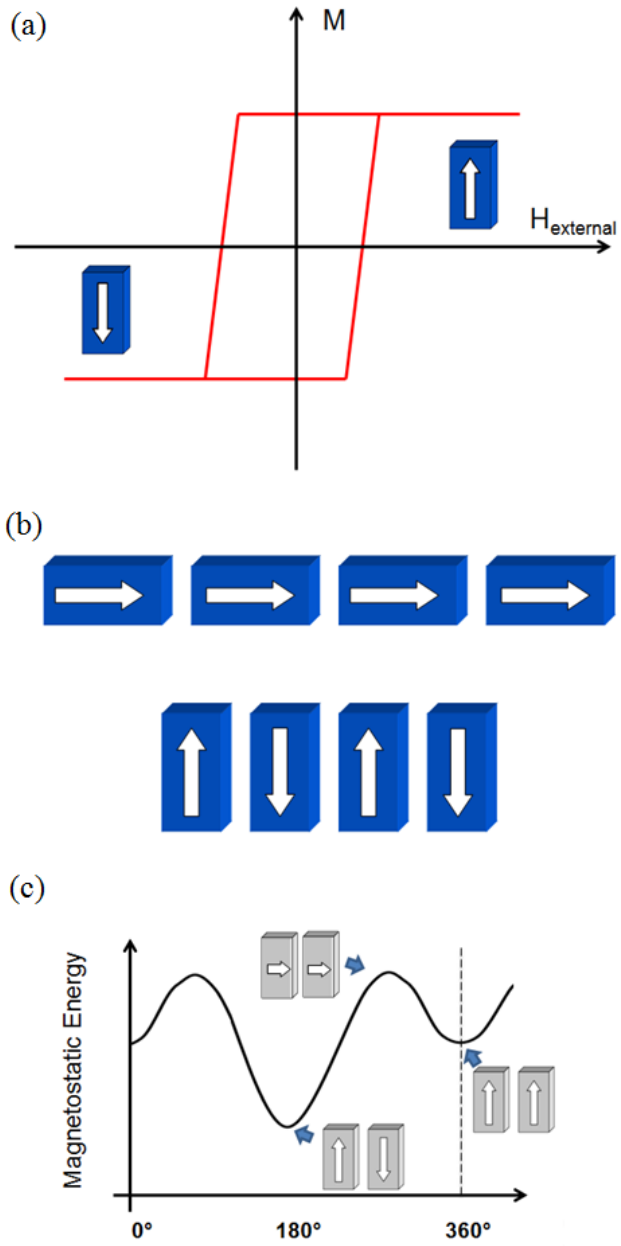

Figure 4: (a) A hysteresis curve of a rectangular single domain cell. (b) Ferromagnetic coupling and antiferromagnetic coupling effects. (c) The energy diagram of two coupled cells as a function of their angular magnetization difference.

A study is presented below to understand the effects of crystalline (versus shape induced) anisotropy, both in-plane and out-of-plane, on the performance of logic channels [25]. Particularly, similarities were drawn between popular nanocells with in-plane shape-

induced anisotropy, e.g., made of Permalloy, and devices with in-plane crystalline anisotropy. The similarity implies interchangeability between these two types of elementary components. However, unlike the shape anisotropy, the intrinsic crystalline anisotropy is not sensitive to the size and shape non-uniformities of nanocells due to an imperfect manufacturing process. Such approach can open a route to efficient scalability into 2-3 nm cell size [26]. In comparison, manufacturing of nanocells made of soft magnetic materials is limited to a 30-50 nm cell size [27,28]. In addition, the ability to select from a great host of available materials with a significant magneto-crystalline anisotropy ensures immunity to thermal fluctuations for many technology generations ahead.

Furthermore, for a material with an out-of-plane anisotropy, even more advantages can be foreseen. The first and most important, conventional 2D networks of magnetic nanocells can be extended into 3D space based on this architecture (Figure 5). Previously, it has been shown that by controlling the interplay of the magnetostatic and quantum-mechanical ("exchange") interaction, reading and writing magnetic information not only from localized regions within a generic 2-D plane but also from individual layers across the thickness - in other words, benefit from a 3rd physical dimension [29]. Similarly, it is possible to exploit individual layers in a 3-D media to vertically place magnetic logic elements. Nanocells with out-of-plane anisotropy can be obtained through stacking Co/Pd or/and Co/Pt multilayers.

The out-of-plane anisotropy here is defined by the quantum-mechanical exchange coupling between adjacent layers. By changing the number of these multilayers, the

magnitude of crystalline anisotropy can be easily controlled. Also, the exchange coupling can be directly adjusted through altering the composition of multilayer stacks. In analogy with magnetic recording technologies, which recently transitioned from longitudinal to perpendicular recording, perpendicular coupling effects also alleviate patterning of nanocells in longitudinal planes. For the same reasons as in magnetic recording, nanocells with an out-of-plane anisotropy have negligible demagnetization field in in-plane transitions and therefore tend to promote substantially higher packing densities compared to materials with in-plane anisotropy including both shape-induced and magneto-crystalline films with in-plane anisotropy [30].

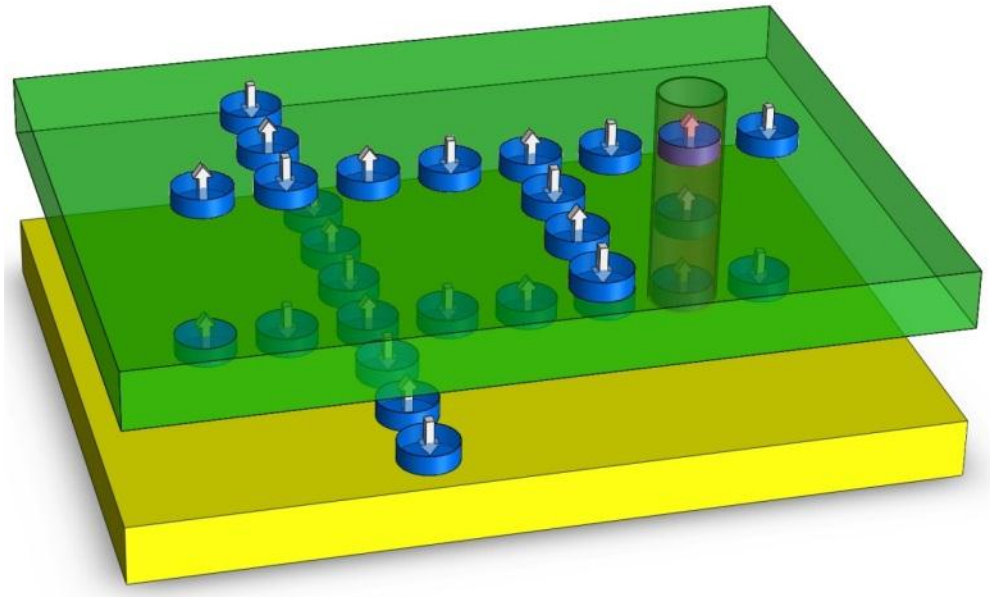

Figure 5: A schematic of a 3D nanomagnetic logic device. Logic components are placed on two different planes. Communication between components on different planes is carried out through a vertical channel of nanocells (marked as a read tube).

Besides, it is one dimension less to deal with when manufacturing magnetic structures with out-of-plane anisotropy compared to those with in-plane anisotropy. For instance, manufacturing perpendicular magnetic recording media, e.g., Co/Pd multilayers, with a

misalignment error of less than 1 percent is a standard deposition process while having a longitudinal media with comparable magnetization alignment accuracy within a plane is a challenge.

Other Magnetic Logic Systems

Besides MQCA, there are two other main magnetic logic implementations: magnetic tunnel junction (MTJ) and magnetic domain wall logic systems (Figure 6).

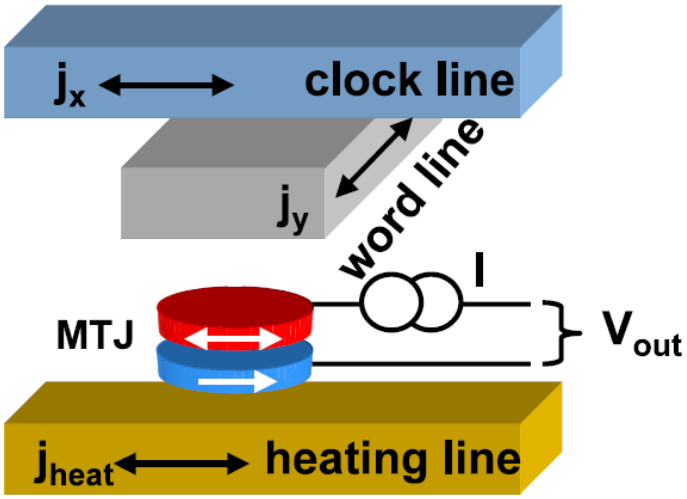

Figure 6: Logic based on single magnetic tunnel junction element [31]. The clock line and word line are two inputs, while the heating line is used to reduce required switching current

Figure 6 shows a MTJ logic unit [31]. The inputs are two wires above the MTJ [32], and optionally a current-carrying line heating the cell. The output is the voltage drop across the magnetic tunnel. Driving current through input wires close to the MTJ will create a magnetic field that can switch the magnetization of the MTJ's soft electrode [33]. Heating the MTJ allows the hard electrode to be magnetically switched. The heat is used to reduce required current. A disadvantage of these schemes is that high current densities

must be switched every time the data change, which is a process requiring high magneto-resistance ratios and large transistors.

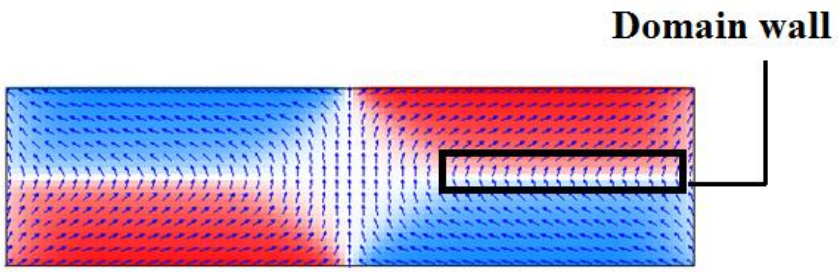

Figure 7: Domain wall separates areas of different magnetizations

A domain wall (Figure 8) is a mobile interface between regions of oppositely aligned magnetization. Domain walls can be propagated through complex network using domain wall propagation s of nanowires under the action of an externally applied magnetic field (Figure 8) [34,35,36]. But the conflict between domain wall directions is the biggest problem for this logic technology. These conflicts can significantly reduce the signal speed [37,38].

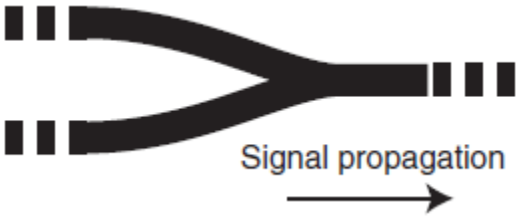

Figure 8: Magnetic domain wall logic gate (NOT)

Soft magnetic material such as Permalloy ($Ni_{80}Fe_{20}$) has been shown to form an excellent conduit for domain walls. The high shape anisotropy of the nanowire ensures that magnetization prefers to align with the long axis of the wire. These two possible

directions form the basis of the binary information representation, with a magnetic domain wall acting as the transition edge in a changing signal. Domain walls can be propagated through complex networks of nanowires under the action of an externally applied magnetic field.

MQCA Devices

To perform binary information storage and computing, two main functionalities are required to be realized: data channel for signal propagation and logic gates for Boolean functions. It has been proved that networks of MQCA can implement both of these functionalities.

Binary Wire (Magnetic Data Channel)

Binary wire is a linear arrangement of nanomagnets coupled only to their nearest neighbors. Both ferromagnetic and anti-ferromagnetic coupled channels can be used for propagating information (Figure 9). The difference is that depends on the number of the nanomagnets made up of the channel, an anti-ferromagnetic coupled channel can be used to not only propagate information, but also invert binary information. More simulation results and analysis will be introduced later.

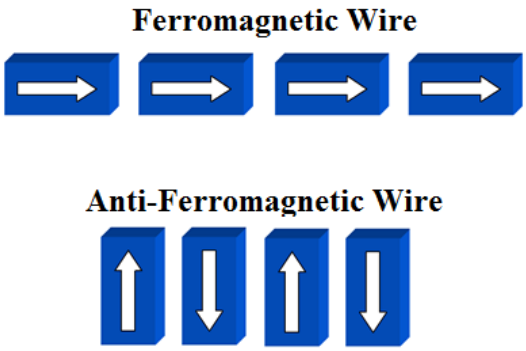

Figure 9: Abstract paradigm of ferromagnetic (above) and anti-ferromagnetic (bottom) coupled data channels.

Universal Logic Gates

It is known that any Boolean logic function can be built by assembling a network of majority gates of NOR and/or NAND. A. Orlov et al. demonstrated a structure of MQCA majority logic gate capable of realizing NOR and NAND logic computing [21]. Such a three-input majority logic gate can be viewed as a programmable two-input (for example, pad A and pad C) NAND or NOR gate, depending on the state of the third input nanocell (pad B).

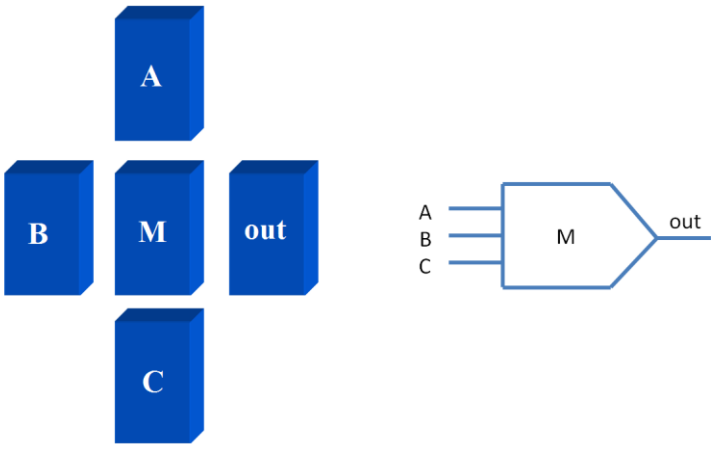

Figure 10: Physical layout and schematic representation for a planar MQCA majority gate; Magnetic state of cell B determines whether the logic function is NOR or NAND.

The truth table of the MQCA majority gate is listed below (Table 1). Determined by the magnetic state of input B, NOR or NAND logic can be realized.

Input B	Input A	Input C	out	
0	0	0	1	N
0	0	1	0	O
0	1	0	0	R
0	1	1	0	
1	0	0	1	N
1	0	1	1	A
1	1	0	1	N
1	1	1	0	D

Table 1: Truth table of the MQCA majority gate.

One of the challenges for application of the real world MQCA is the need for coupling of external signals to the nanomagnets (e.g., coming from CMOS part of the circuit).Such electric-to-magnetic signal converters to be used to switch the drivers independently are not developed yet.

Research Focus

The ultimate goal of my research is to develop high density, non-volatile magnetic logic devices for computing and information storage. To increase density, extend conventional magnetic quantum-dot array (MQCA) networks to the third-dimension is a great option. I proved the feasibility of building three-dimensional magnetic logic devices with MQCA composed with materials with crystalline anisotropy. Further applications, high density

magnetic recording system and universal majority logic gates, were fabricated. Their magnetic properties were measured and discussed. Magnetic tunnel junction (MTJ) with perpendicular magnetization is another interesting field. Simulation of MTJ for information storage was presented. Furthermore, an extended research of spin-transfer Torque (STT) Magnetization reversal in sub-10-nm magnetic tunneling junction point contacts was demonstrated. The results showed significant reduction of required switching current.

Chapter 2 Magnetics Study of Permalloy MQCA Channels

Micromagnetism Theory

The Landau-Lifshitz-Gilbert (LLG) equation [39] is a classical differential equation descripts the motion of magnetization **M** at nanoscale:

$$\frac{d\boldsymbol{M}}{dt} = -\gamma \boldsymbol{M} \times \boldsymbol{H}_{eff} - \frac{\gamma\alpha}{M_s} \boldsymbol{M} \times (\boldsymbol{M} \times \boldsymbol{H}_{eff})$$

In this equation, **M** and $\mathbf{H}_{\text{eff}}$ are vectors, which represent the magnetization and effective magnetic field, respectively, γ is the gyromagnetic ratio, α is the damping coefficient, and Ms is the saturation magnetization of the material under study. The effective field $\mathbf{H}_{\text{eff}}$ is derived from the superposition of interactions between spins. The four interactions are: (1) exchange energy, due to exchange interactions; (2) Anisotropy energy, due to crystalline or shape anisotropy; (3) Demagnetization energy, due to self-demagnetizing fields; (4) Zeeman energy, due to interaction with the applied field. The effective field $\mathbf{H}_{\text{eff}}$ can be obtained from the total energy of the magnetic system according to the following equation:

$$H_{eff} = -\mu_0^{-1} \frac{\partial \boldsymbol{E}}{\partial \boldsymbol{M}}$$

OOMMF is used to solve these equations with respect to local magnetization vectors ("spins"). The angular dependence of the system energy is plotted to understand the bi-stability and energy barrier between ground and metastable states, as illustrated in Figure 4b and Figure 4c. The damping term is taken into account since that energy is exchanged with the environment (Figure 11), thus the magnetization loses energy over time and tends to align with the field vector of the effective magnetic field.

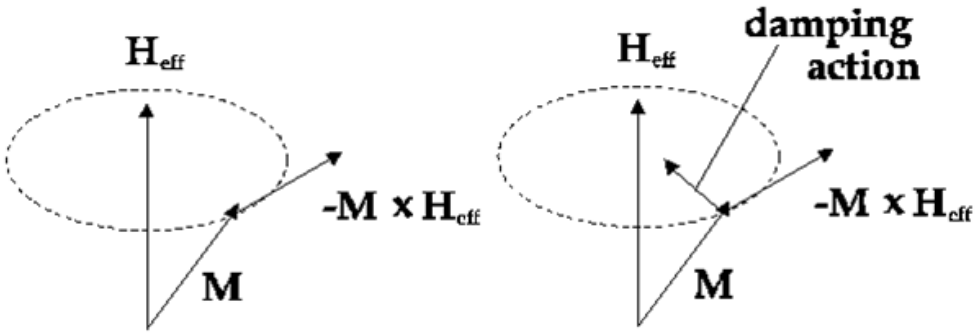

Figure 11: Schematics of undamped gyromagnetic precession (left) and damped gyromagnetic precession (right).

Model Description

A popular public-domain micro-magnetic simulation software package, Object Oriented MicroMagnetic Framework (OOMMF) [40], was used to study magnetic properties of magnetic devices under study. OOMMF simulates magnetic models based on the Landau-Lifshitz-Gilbert equation.

Figure 12: Logo of Object Oriented MicroMagnetic Framework (OOMMF)

Models were simulated to investigate the effects of several essential components of a MQCA data channel. All nanomagnets are small pads made of permalloy. It means that these nanocells have no crystalline anisotropy energy, but only shape anisotropy. The

saturation magnetization was set to 8×10^5 A/m (860 emu/cubic centimeter). The mesh size was 5 x 5 x 10 nm^3.

Results and Discussion

The first model reveals the effect of shape anisotropy. The channel made up with circular nanocells shows very little coupling effect, while the rectangular channel is fully antferromagnetic coupled. This result indicates that the magnetic field of a nanocell is not strong enough to switch its neighbor. Shape anisotropy let the rectangular pads have the tendency to align their magnetization to their long axis.

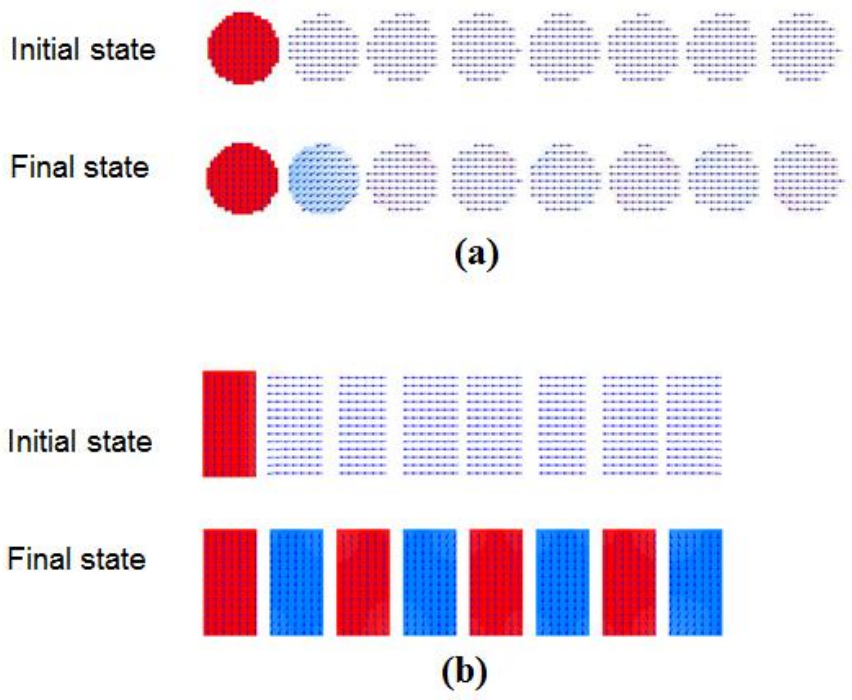

Figure 13: (a) Circular nanocell channel (diameter = 40 nm, thickness= 15nm, Spacing = 5 nm); (b) Rectangular nanocell channel (40x80x20 nm3, Spacing = 10nm).

The second model shows ferromagnetic coupling effect. The first nanocell was initialized to fully align to its easy axis while the rest cells were saturated to their hard axis. Once the simulation started, the signal was correctly propagated through the whole data channel.

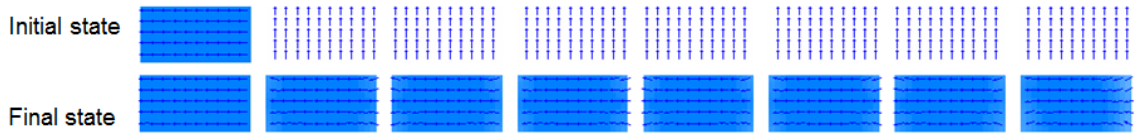

Figure 14: Simulation of a ferromagnetically coupled MQCA data channel. Nanocells were of 50 x 100 x 30 nm^3; spacing was15nm.

The third model was designed to present an example of misalignment. Misalignment, sometimes called misordering, is a case that nanocells are not correctly coupled. The fact is that even not affected by any external magnetic field (for example, the input signal), nanocells trend to align their magnetization to the easy axis by themselves. This is due to their anisotropy energy. Plus, a nanocell may be affected by long range dipole interactions from magnets further than its two neighbors, which is another source of misordering. Figure 15 shows the misalignment happened in an antiferromagnetically coupled data channel.

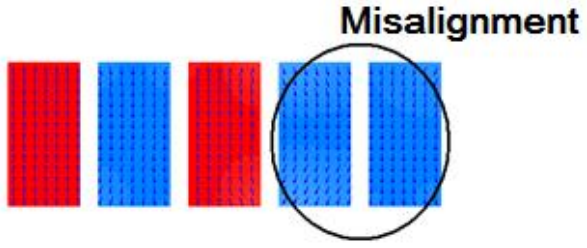

Figure 15: Misaligned nanocells in an antiferromagnetically coupled MQCA data channel. The last cell shall have different magnetization to the second-last one.

The thickness of nanocells is another essential factor of shape anisotropy. If a nanomagnet is too thick, it cannot maintain single domain property (Figure 16a). On the other hand, if nanocells are too thin, they will be too easily rotated by long range interactions. Figure 16b shows the misalignments caused by long range interactions. Based on large amount of simulations, it was found that for nanomagnet of 50 nm x 100 nm, the proper thickness range is 20 to 30 nm (Figure 16c).

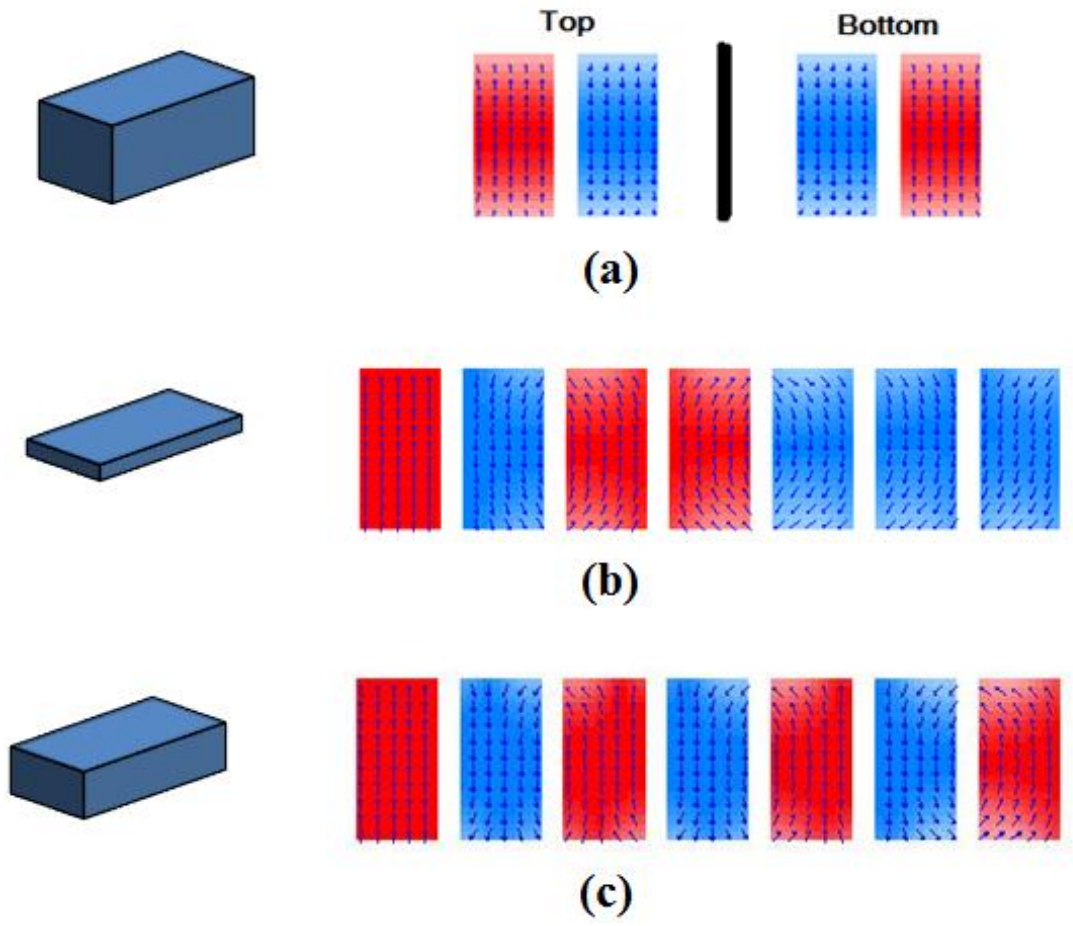

Figure 16 Effect of nanocell thickness. The models had different thicknesses of (a) 50 nm; (b) 10 nm; (c) 30 nm. Spacing was 15nm. Length and width were 50nm and 100nm, respectively.

Figure 17 shows a model to investigate the effect of holding fields. Holding field is a uniform external field applied to the whole MQCA network with direction identical to the hard axis of a nanocell. A holding field can prevent the self-misalignment and let signal correctly pass through more nanocells.

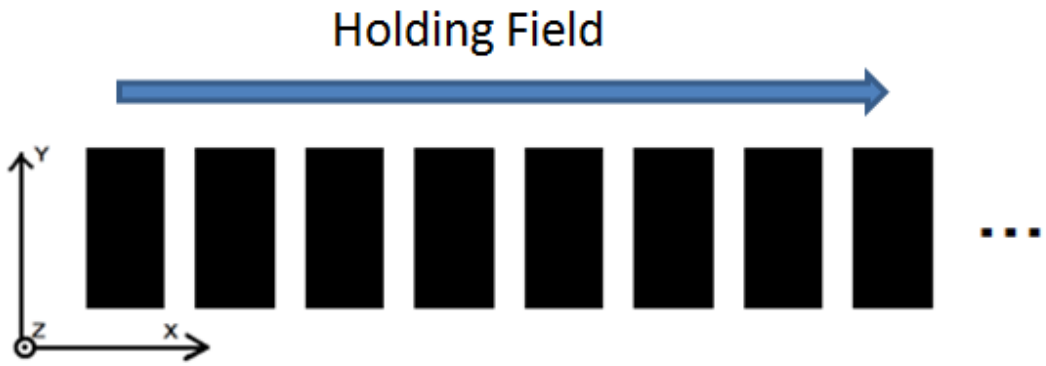

Figure 17: Illustration of the holding field. It has the same direction with the hard axis of the nanocells.

However, the holding field will also add some suppressing effect to signal propagation. There is a trade-off between signal propagation speed and propagation distance. Judging by the results, several conclusions can be summed up. If the holding field is too small, too few pads will be propagated before meeting a misodering. Actually, before the first misordering finally happens, there are some nanocells have obvious tendency to misorder, but fixed by the incoming signal. Somehow, this kind of fixing slows the signal speed. To avoid this effect, I started my tests from 15mT, in order to have enough proper pads to show the result. When the holding field is too big, signal speed is significantly reduced. If the holding field is made even bigger, the signal transportation will be stopped after passing through several pads. Of course, under this situation, propagation ability is

reduced too. This is easy to understand, since the holding field is too large for the magnetic coupling effect.

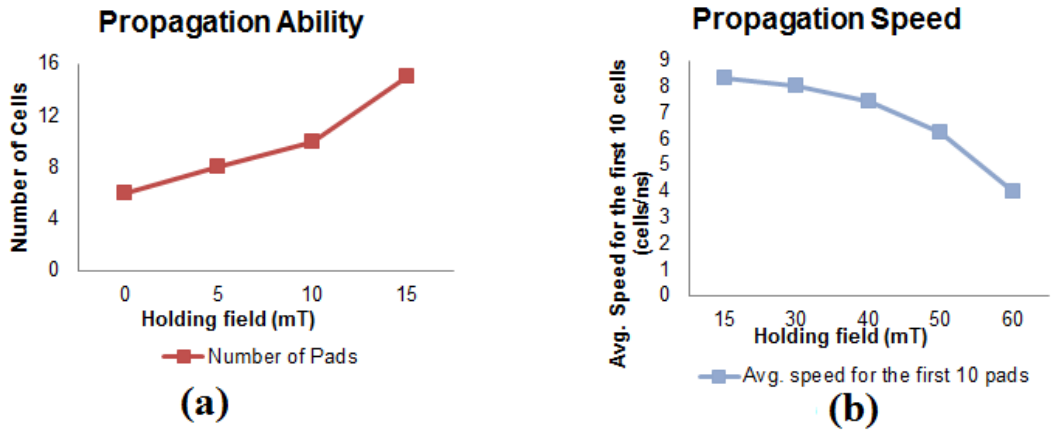

Figure 18: Effects of holding field. There is a trade-off between signal propagation speed and correct propagation distance (before any misalignment happened).

In summary, holding field can have signals propagate further, meanwhile reduces the signal speed. How to compromise these two factors depends on the specific needs.

Chapter 3 Simulation of Signal Propagation in MQCA Channels Composed of Material with Crystalline Anisotropy

Conventional MQCA elements are made of material have no crystalline anisotropy. It was a novel field to explore if crystalline anisotropy can archive similar features as shape anisotropy in building MQCA elements.

Model Description

a) Nanocells with In-plane Crystalline Anisotropy

A schematic of a typical data channel with circular (shape-free) cells in this modeling study is shown in Figure 19b. In the simulations of the bi-stability or the energy diagram, only the first two cells are analyzed. Again, circular shape cells were used to eliminate any shape dependence. Each cell had a diameter of 50 nm and a thickness of 5 nm. The saturation magnetization and the exchange energy constant were modeled to be 8.6×10^5 A/m and 1.3×10^{-11} J/m, respectively, i.e., comparable to the values for Permalloy [41,42]. All elements were modeled to have a uniaxial crystalline anisotropy along Y axis. The mesh element had dimensions of $2 \times 2 \times 5$ nm^3. Other parameters, such as the spacing, the anisotropy energy density, etc., were treated as input variables.

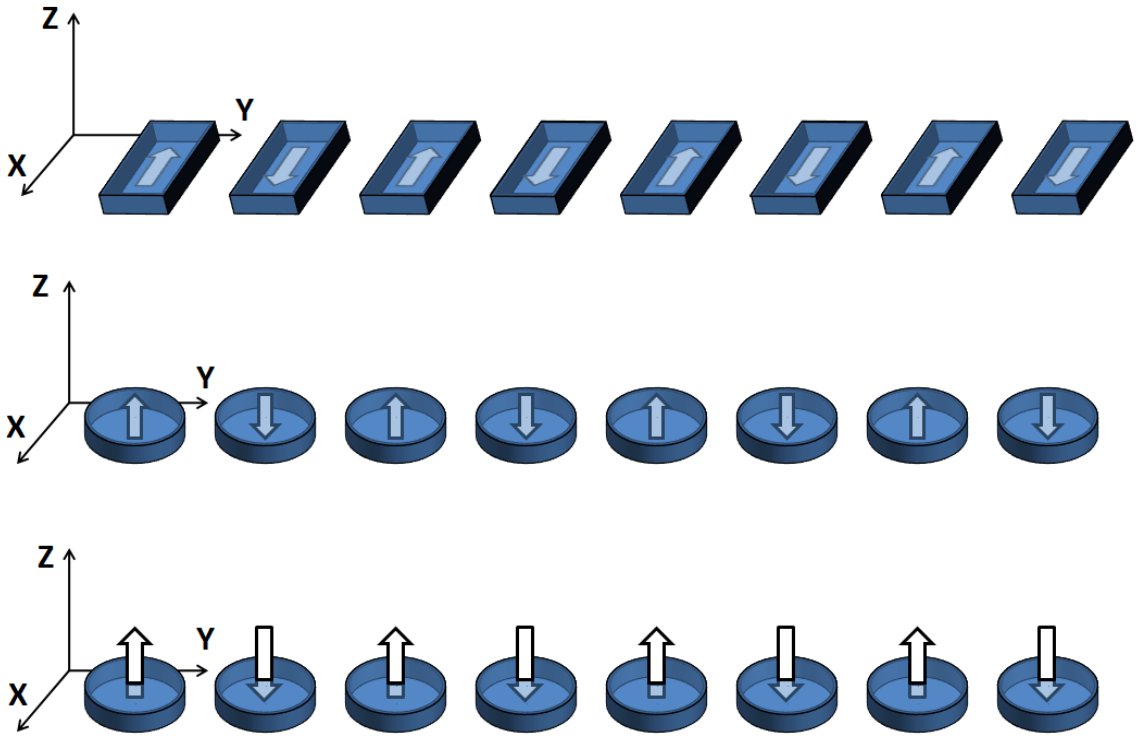

Figure 19: Schematics of nanomagnetic data channels and the coordinate system definition for (a) shape-induced in-plane anisotropy (b) crystalline in-plane anisotropy channel and (c) crystalline out-of-plane anisotropy channel.

b) Nanocells with Out-of-plane Crystalline Anisotropy

Figure 19c illustrates a nanomagnetic data channel with an out-of-plane crystalline anisotropy. In this model, each nanocell had a cylindrical shape with a 60 nm diameter and a 20 nm height. The saturation magnetization, Ms, and the exchange energy constant were set to be 5.4×10^{5} A/m and 1.3×10^{-11} J/m, respectively. These values are similar to those for exchange-coupled Co/Pt (or Co/Pd) multilayers, some of the popular materials with out-of-plane anisotropy as used in conventional perpendicular magnetic recording [43]. Garnet is another material which could be potentially used for this particular

application [44]. Garnet films are known to be relatively cost-effective and extremely high quality.

Results and Discussion

As introduced above, magnetic bistability and the capacity of performing ferromagnetic and/or antiferromagnetic coupling effects are decisive features for qualified nanocells used to form magnetic logic devices. To prove the feasibilities of our novel types of nanocells, simulation models are ingeniously designed to examine these crucial characteristics. Thereafter, the propagation speed and reliability of a data channel are investigated, and their internal relation is revealed. The 3D expansibility of nanocells with out-of-plane anisotropy is further expatiated as well based on simulation results.

a) Bistability

To properly represent binary "0"-s and "1"-s, each nanocell should have two stable states of magnetization. In order to verify the bistability, a nanocell is placed in a varying magnetic field to have its magnetization direction gradually rotated by 360° within the z-plane. After the energy status of each nanocell is acquired, the computation is performed to reveal the influence of magnetization angle difference. Upper and bottom sides of Figure 20 show simulated energy diagrams of a single nanocell with in-plane and out-of-plane crystalline anisotropy, respectively.

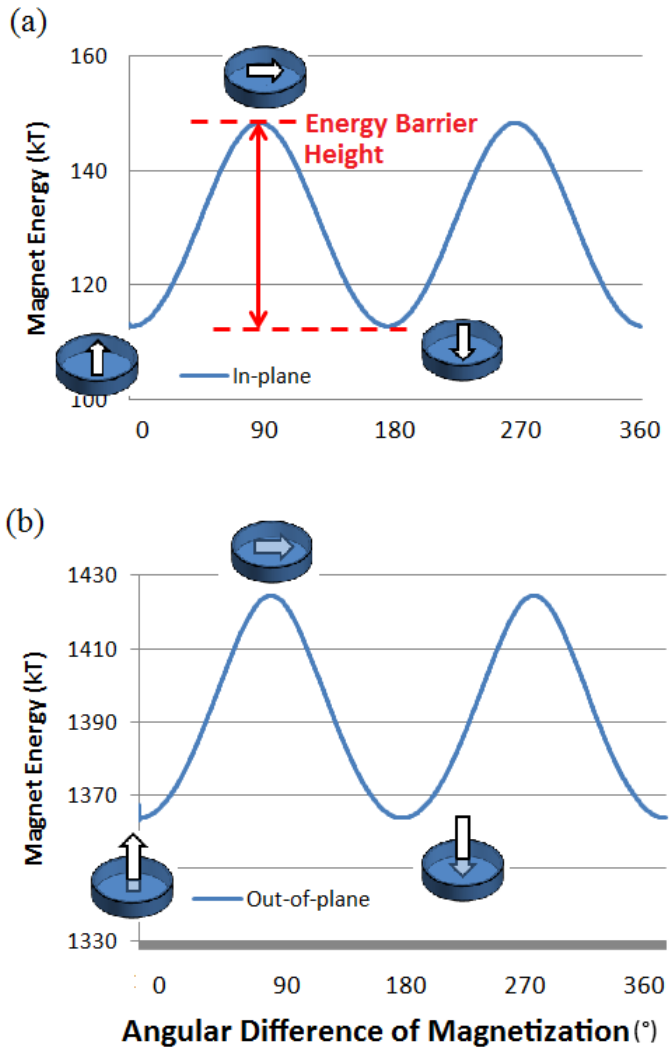

Figure 20: Simulated energy diagrams for cells with in-plane (up) and out-of-plane anisotropy (down).

As expected, the energy diagrams indicate that when the magnetization in each cell rotates by 0 and 180 degrees with respect to the "easy" axis, the nanocell is in one of its two lowest energy states, respectively. The difference between the energy peak and the adjacent bottom is regarded as an energy barrier. It represents not only the power dissipation of this nanocell, but also the stability of information stored in it. Ambient thermal fluctuation is a potential threat that may disturb system operation. Every time the

volume of a nanocell is reduced to comply with scaling, the height of the barrier is also reduced. For microsecond stability, an energy barrier of 0.26eV is enough [45,46,47].

Not to mention, choosing material with higher out-of-plane anisotropy can further increase the energy barrier and consequently improve the stability. It is worth noticing that magnetic logic devices can normally function with substantially looser requirements on stability compared to those for information storage. For proper gate operation, logic elements are required to maintain their stability only during nanoseconds of the operating time. Thus, nanocells with out-of-plane anisotropy can be scaled down to sub-10-nm range.

b) Magnetic Coupling Effects

This section focuses on proving that both types of novel nanocells, no matter with in- or out-of-plane crystalline anisotropy, can perform decent in-plane magnetic coupling effects to build 2D networks of nanomagnets (PNON). The ability of nanocells with out-of-plane anisotropy to possess perpendicular magnetic coupling interaction in 3D space is discussed later in another section of this article.

For two adjacent in-plane ferromagnetically (parallel) or antiferromagnetically (anti-parallel) coupled nanocells, the coupled energy diagrams are shown on upper and lower sides of Figure 21, respectively. Here, the in-plane anisotropy direction (“easy” axis) is chosen normal to the channel axis to trigger anti-parallel coupling. This provides equivalent comparison with the out-of-plane orientation which is always anti-parallel in this configuration.

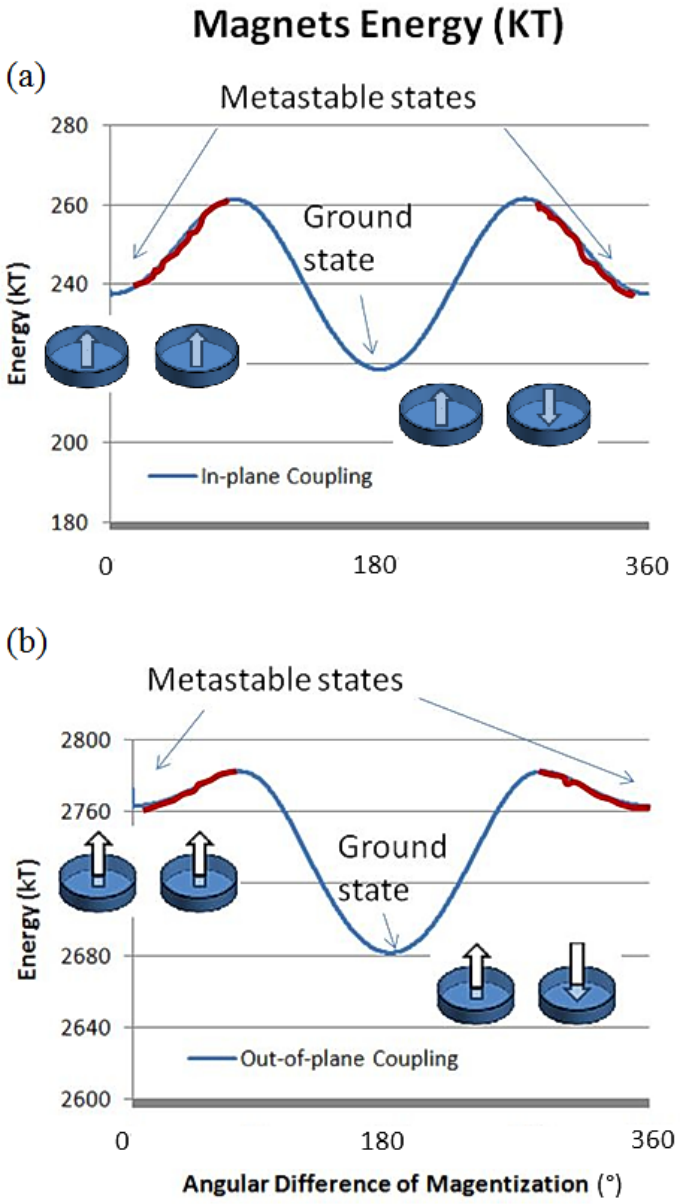

Figure 21: Energy diagram of ground and metastable states for two coupled nanocells with in- or out-of-plane (down) crystalline anisotropy. Red side lines show energy barriers separating metastable states.

The separation between two adjacent in-plane and out-of-plane coupled nanocells was modeled to be 10 and 20 nm, respectively. Both energy diagrams clearly indicate

similarity between the shape-free nanocells with crystalline anisotropy and previously studied shape defined Permalloy nanocells. Another important situation can be observed from the diagrams is related to the energy states themselves. Besides the global minimum state corresponding to the anti-ferromagnetic ground state, it can be seen that the adjacent local minima corresponding to ferromagnetic coupling. These local states define the metastable states which should be avoided at least in the initial phase of magnetic logic development. Therefore, one of the important tasks of the magnetic logic device optimization is the minimization or complete elimination of the energy barriers separating the metastable states from the nearest ground state (shown by red lines in Figure 21).

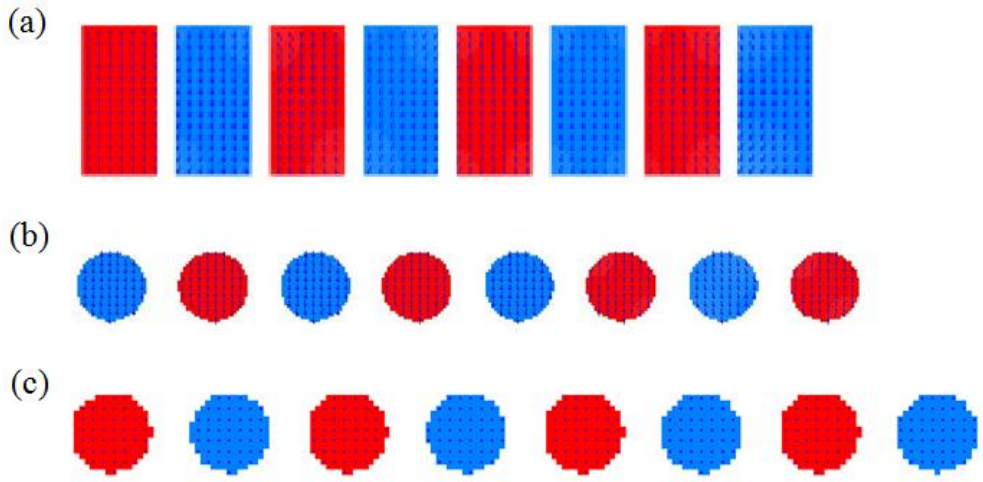

Figure 22: Signal propagation through antiferromagnetically coupled data channels of the following three types: (a) A conventional channel with a shape-driven anisotropy. (b) A channel with in-plane anisotropy normal to the axis of the channel. (c) A channel with an out-of-plane crystalline anisotropy.

The process of signal propagation through a nanomagnetic data channel is illustrated in Figure 22. Here, the arrows indicate the magnetization direction; the depth of color in each portion of a nanocell shows the strength of the magnetization. Red side lines show

energy barriers separating the two side metastable states from the ground state. In the initial state, the magnetization in each nanocell, with the exception of the first one, is saturated along the hard axis, i.e., in this case along the channel direction. The first nanocell would be used as an input terminal and its magnetization switched to “down” represents “0”.

c) Trade-off between Reliability and Data Rate

The possible magnetic states in a channel of bi-stable nanocells are affected by a host of factors. The goal of the magnetic logic design is to learn to control these states and improve device characteristics related to its operation and reliability. For instance, the anisotropy is one of the major factors to influence the dynamics of the channel. Higher anisotropy facilitates switching to ground states and therefore results in an increased data rate. However, higher anisotropy also requires higher magnetic field to trigger switching. In turn, if no external field sources are exploited, a higher recording field calls for a higher saturation moment which generates a higher demagnetization field and therefore causes destabilization of the magnetic state. The trade-off can be resolved through numerical simulation optimization. Figure 23 illustrates the effects of anisotropy, nanocell thickness, and saturation magnetization.

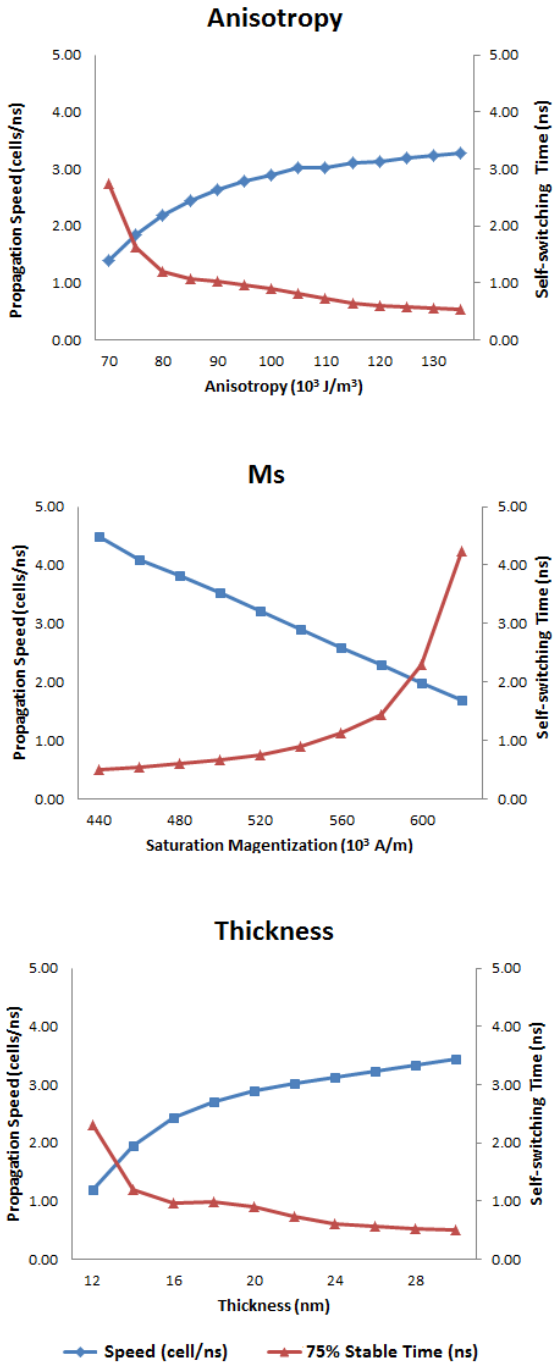

Figure 23: The comparison between magnetization stability and signal speed versus the change of (a) Anisotropy; (b) Saturation magnetization (Ms); (c) Thickness.

Figure 23a indicates acceleration of the propagation speed and a drop of the characteristic switching time with an increase of the anisotropy constant. These tendencies can be

foreseen since greater anisotropy helps a nanocell fall into ground states. Conversely, the increase of the saturation magnetization (Ms) enhances the hardness of a nanocell against magnetization changing. Therefore, it leads to a decline of the propagation speed and a prolonging the switching process, as illustrated in Figure 23b. Figure 23c indicates that the increase of nanocell thickness results in a higher propagation speed and less stability. Such dependence can be explained by the increased directional dispersion of the magnetization with an increase of the thickness.

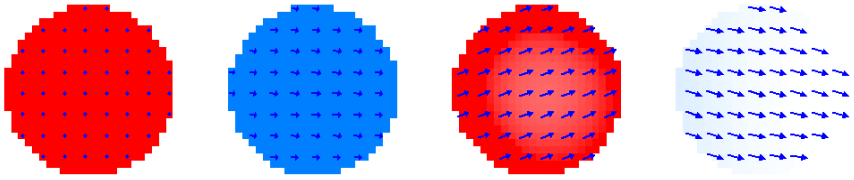

Figure 24: A moment of signal propagation process. Only the input cell was completely saturated. Although the second and third cells had not finished switching, binary signal can still be propagated through them.

To quantify the notion of stability as it relates to this particular application, the characteristic time, which is necessary for an individual nanocell to align its magnetization with no any external field present, is used as the criterion. This time quantum is obtained by simulating a one-nanocell model. Generally, before a nanocell is fully saturated, the stray field by the cell itself will be large enough to trigger magnetization switching of the next cell in the channel (Figure 24). Thus, the timing will be stopped once the nanocell reaches 75% maximum magnetization along its “easy” direction. In the past, researchers chose to simply count the number of cells before any misalignment happens. However, according to this model, it is not trivial to comprehend the true stability of the system. Because the self-driven switching of two adjacent

nanocells may arbitrarily have opposite or same directions, both of these switching processes will be either reinforced or suppressed (Figure 25), respectively. As a result, the distance of successful propagation may be expanded or reduced merely by coincidence. On the contrary, the study of a single nanomagnet can eliminate this uncertainty.

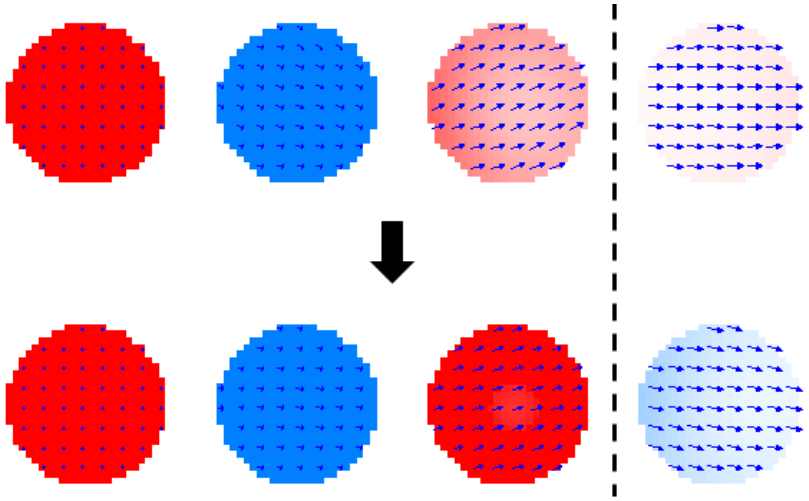

Figure 25: A typical suppressed propagation process. The magnetization of the last cell spontaneously starts to into same direction as its neighbor. Although it is "corrected" later by the input signal, this condition slows regular propagation speed.

d) Three-Dimensional Expansibility and Interlayer Cross-talk of Nanocells with Out-of-plane Anisotropy

Unlike nanocells with in-plane anisotropy which can create only in-plane magnetic coupling effects, nanocells with out-of-plane anisotropy are capable of performing both in- and/or out-of-plane magnetic coupling interactions.

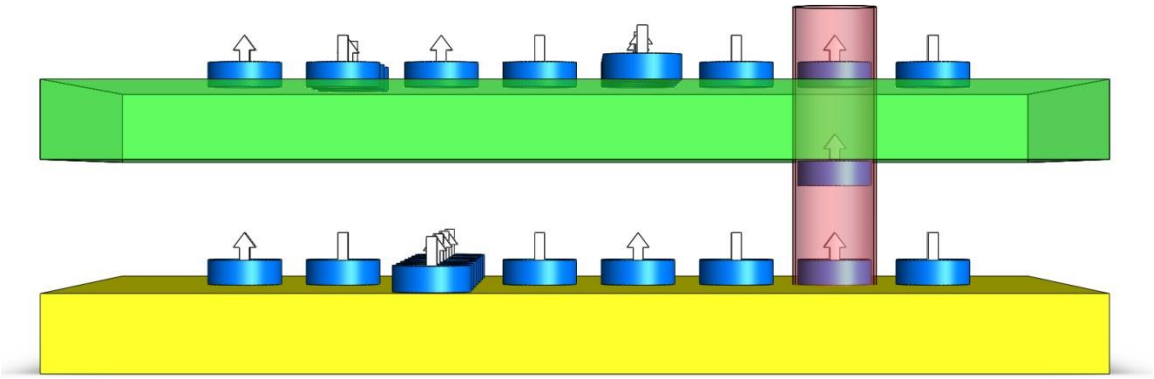

Figure 26: A schematic view of a three-dimensional nanomagnetic logic device. Nanocells within the red tube form a vertical data channel.

As shown in Figure 27, nanocell A, B and C are out-of-plane cells with identical magnetic parameters. Here, Cell A is the input unit, which is already saturated at the initial stage. Similar to the data channel mentioned above, Cell B is placed next to A at the same horizontal level (x-y plane). However, Cell C is vertically above A and therefore extends this device into a 3D architecture. The magnetic state within Cell A can influence magnetic states within both Cell B and Cell C. Images (a) through (d) reveal the time dependence of the underlying switching processes.

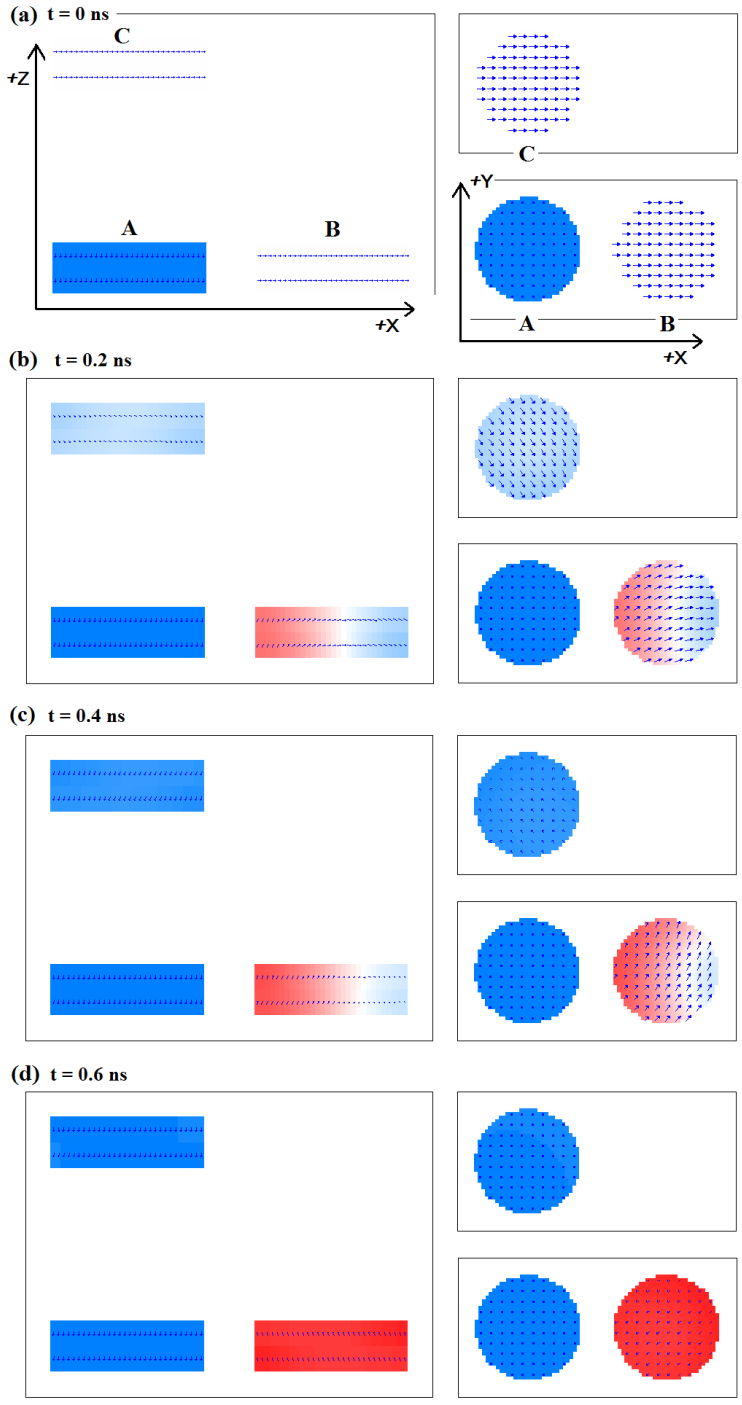

Figure 27: An implementation of out-of-plane 3D nanomagnetic logic. All nanocells are made of the same out-of-plane anisotropy material. Cells A and B are on the same plane, while cell C is placed above cell A. Each of these cells has a diameter of 60 nm, 10^5 J/m^3 anisotropy, and 5.4 × 10^5 A/m Ms. The mesh size was set to 2 × 2 × 10 nm^3.

In devices made up with out-of-plane nanocells, communication between elements on different planes is performed through chains of ferromagnetically coupled nanocells (namely magnetic wires). A schematic longitudinal section of a 3D logic device is shown in Figure 28.

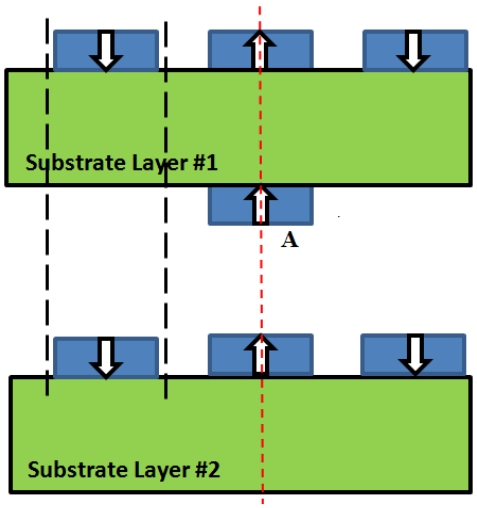

Figure 28: A longitudinal section diagram of a 3D nanomagnetic logic device. For a proper separation, the three nanocells in the middle form a bridge connecting two different networks of logic elements.

In the 3-D case, the signal interference between planes is an open question addressed in the model. To bridge substrate layers 1 and 2, nanocell A is fixed on the back of layer 1. If the separation between layers 1 and 2 is not large enough, nanocells within the black dash lines will interfere with each other. A model was simulated to identify an adequate separation which can eliminate the signal crosstalk. Two nanocells are vertically placed. Cell A is an input cell is initially saturated to "1". Cell B has an initial state close to "NULL", except 1% bias to "0". If the spacing between them is not adequate, magnetization of Cell B will be reversed and end up as the same direction as Cell A, and

vice versa. Simulation results show that for a nanocell with a 30-nm diameter, a 10-nm thickness and a 10^3 J/m^3 anisotropy density, a 70-nm distance is more than enough to avoid crosstalk. Since magnetic logic cells have ultra-low-power consumption compared to silicon transistors, stacking a great number of layers in one nanomagnetic logic unit can be beneficially exploited.

Chapter 4 Simulation of Magnetic Tunnel Junction for Information Storage

Magnetic tunnel junction device with perpendicular magnetization

Magnetic tunnel junction (Figure 29) is a device consisting of two magnetic layers and a barrier layer (insulator) separating them. With this composition, a quantum mechanical magnetoresistive effect called tunnel magnetoresistance (TMR) occurs: electrons in one magnetic layer can tunnel through the insulator [48,49]. Depending on whether the magnetizations in two ferromagnetic layers are parallel or antiparallel, the capability of electrons to tunnel through the barrier layer has a difference [50]. Hence, TMR effect can be utilized to represent two stable electrical resistance states. Electrons are easier to travel between two magnetic thin films if magnetizations of them are parallel. The magnetization of each magnetic layer can be reversed independently through an external magnetic field.

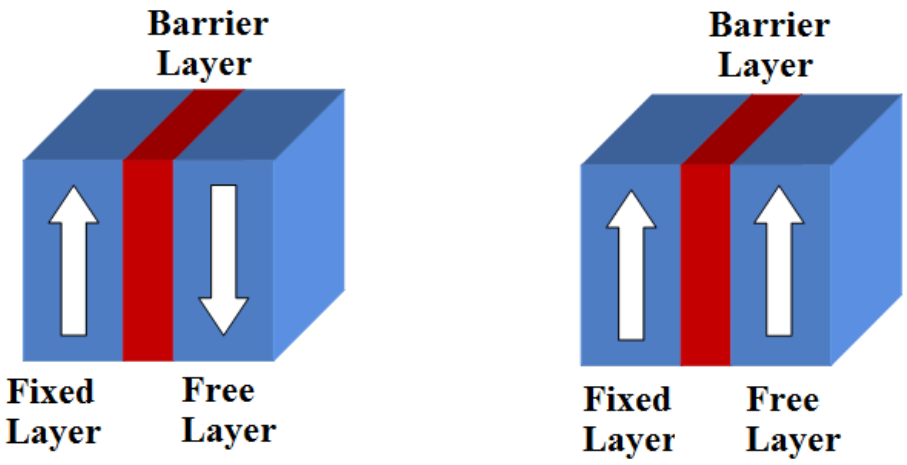

Figure 29: Illustration of Anti-Parallel (left) and Parallel (right) magnetic tunnel junction with in-plane anisotropy.

TMR effect was first discovered in 1975 by M. Julliere [51]. In early stages, magnetic tunnel junction could only operate under extremely low temperature created in laboratory environment [52,53]. Since 1990s, room temperature TMR effect was found and MTJ have been considered as the basis of next generation magnetoresistive random-access memory (MRAM) [54,55]. To advance higher areal density, MTJ with perpendicular anisotropy has gained more and more attraction since the beginning of the twenty-first century [56,57].

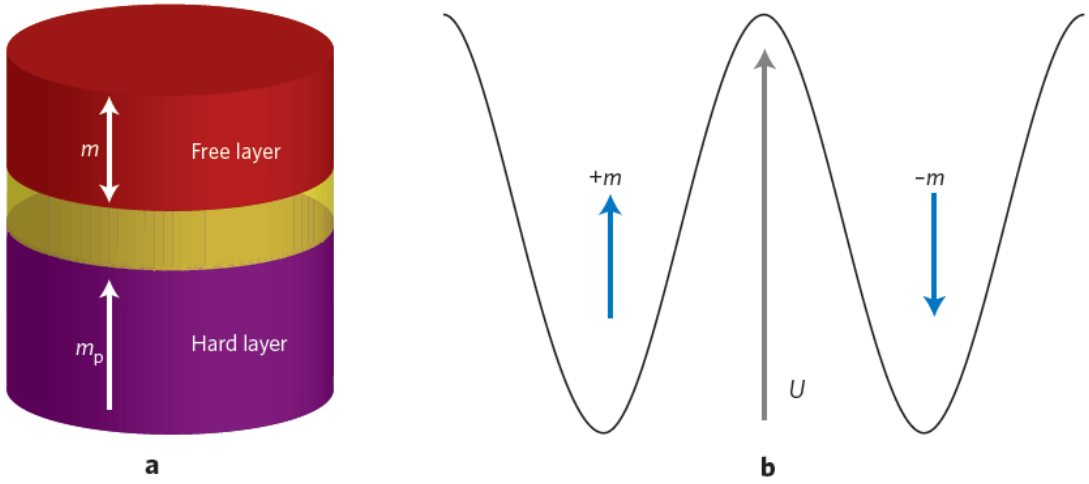

Figure 30: Illustration of perpendicular MTJ [58]. (a) Magnetic tunnel junction with perpendicular magnetized magnetic layers. (b) The energy barrier between parallel and antiparallel magnetization states.

The goal of this simulation is to show that our configuration of perpendicular magnetic tunnel junction (MTJ) is capable of attaining four stable magnetic states, depending on the magnetization directions of the fixed and free magnetic layers. These four states can be later classified as two magetoresistance positions, high and low, which denote binary "0" and "1".

Model Description

The magnetic layers in a MTJ are simulated by two cylinders of different magnetic properties in this model. The upper cylinder (Cylinder 1) is made of Co/Pt with diameter of 75 nm and height of 12 nm. Its saturation magnetization is 8.0×10^5 A/m (800 emu/cc) and anisotropy energy is 6×10^5 J/m^3. The bottom cylinder (Cylinder 2) is 13 nm high, made of Co/Pd, and with 60 nm diameter. Difference in their sizes is due to the reason that in reality, the MTJ will be of a tip-like shape, so the two magnetic layers will not have identical dimensions. The saturation magnetization of cylinder 2 is 1.2×10^6 A/m (1200 emu/cc) while the anisotropy energy density is 10^6 J/m^3.

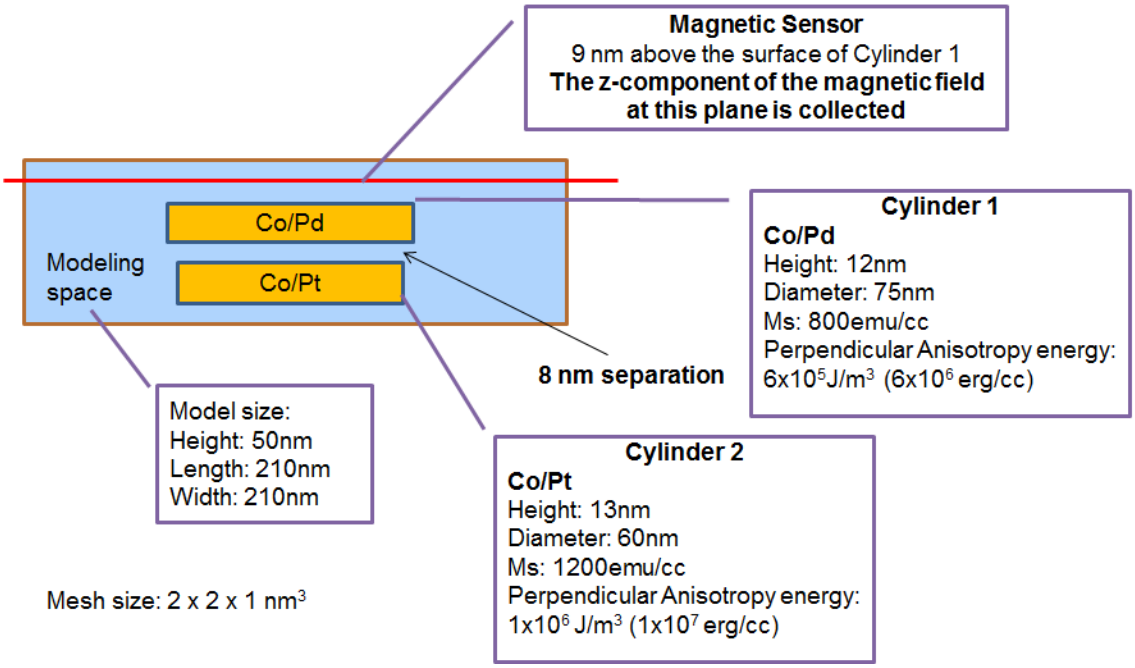

Figure 31: The cross-section diagram and magnetic parameters setup of our perpendicular MTJ model.

The gap between these cylinders is 8 nm wide. It will be filled with non-magnetic material to act as the tunnel barrier. A tunnel barrier is the substance to separate magnetic

layers and the premise of creating magneto tunneling effect. The mesh size of our model is $2 \times 2 \times 1$ nm^3. Magnetic properties in the plane 9 nm above the upper magnetic layer were measured and collected. It is similar as having a magnetic sensor at that position. The cross-section of our model is display above (Figure 31).

Simulation and Results

Simulation was performed with OOMMF, and the data recorded was analyzed, later visualized with MatLab. To describe the model, tcl language was used (Figure 32: Tcl code describing the MTJ dimensions (not the complete code of modeling).).

```
# MIF 2.1
set pi [expr 4*atan(1.0)]
set mu0 [expr 4*$pi*1e-7]
set bd 14e-9

Specify Oxs_ImageAtlas:empty1 {
    xrange {0 110e-9}
    yrange {0 110e-9}
    zrange {0 5e-9}
    viewplane "xy"
    image empty.bmp
    colormap {
        black cobaltone
        white nonmagnetic
    }
    matcherror 0.1
}

Specify Oxs_ImageAtlas:round2 {

Specify Oxs_ImageAtlas:empty2 {

Specify Oxs_ImageAtlas:round1 {

Specify Oxs_ImageAtlas:empty3 {


Specify Oxs_MultiAtlas:cylinder {
    atlas :empty1
    atlas :round2
    atlas :empty2
    atlas :round1
    atlas :empty3
}
```

Figure 32: Tcl code describing the MTJ dimensions (not the complete code of modeling).

Figure 33 displays the initial and final states of four different combinations of magnetization directions. Clearly, due to the tunnel barrier layer, the change is trivial as expected. The red arrows denote the initial setup of magnetization directions in two magnetic layers.

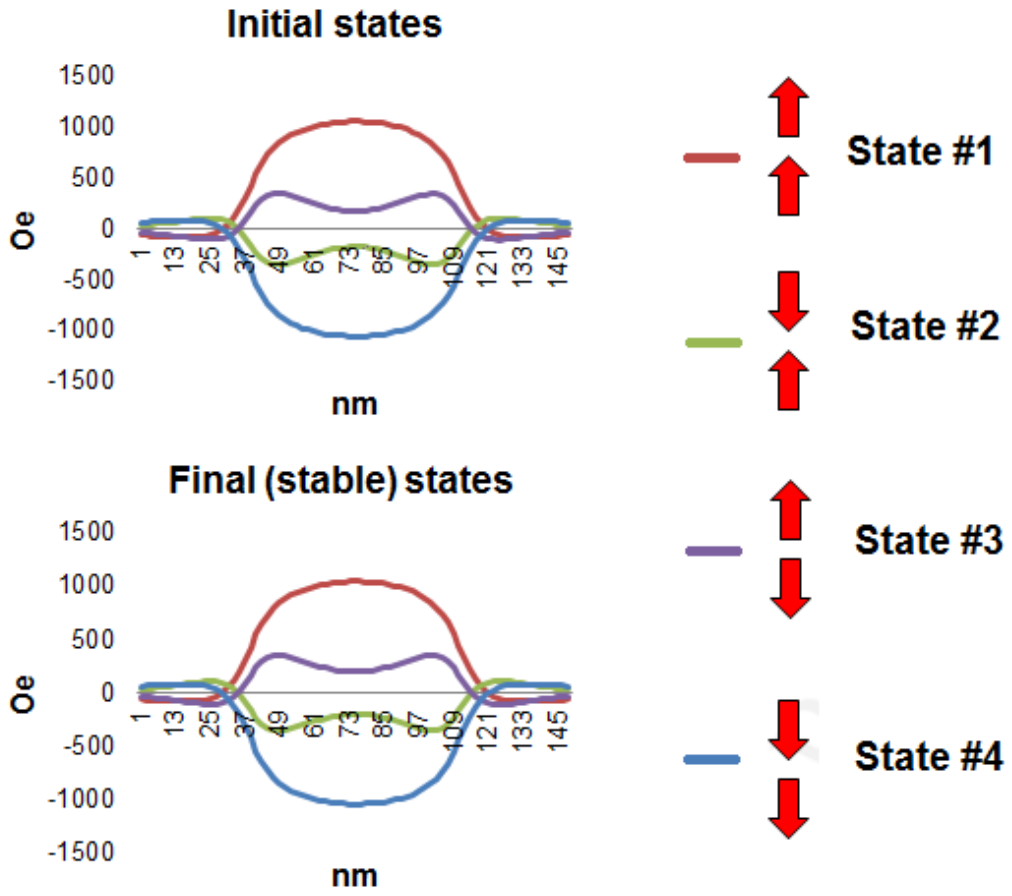

Figure 33: The initial and final states of all four different magnetization combinations. Magnetic changes from initial to final states are trivial.

As shown in Figure 34, four different magnetic stable states can be easily distinguished. State#1 and state#4 will result in high magnetoresistance, meanwhile #2 and #3 will result in low magnetoresistance. High and low magnetoresistance can be used to

represent “0” and “1”, respectively. Simulation results successfully proved the feasibility of using magnetic tunnel junction in our configuration to perform binary information storage.

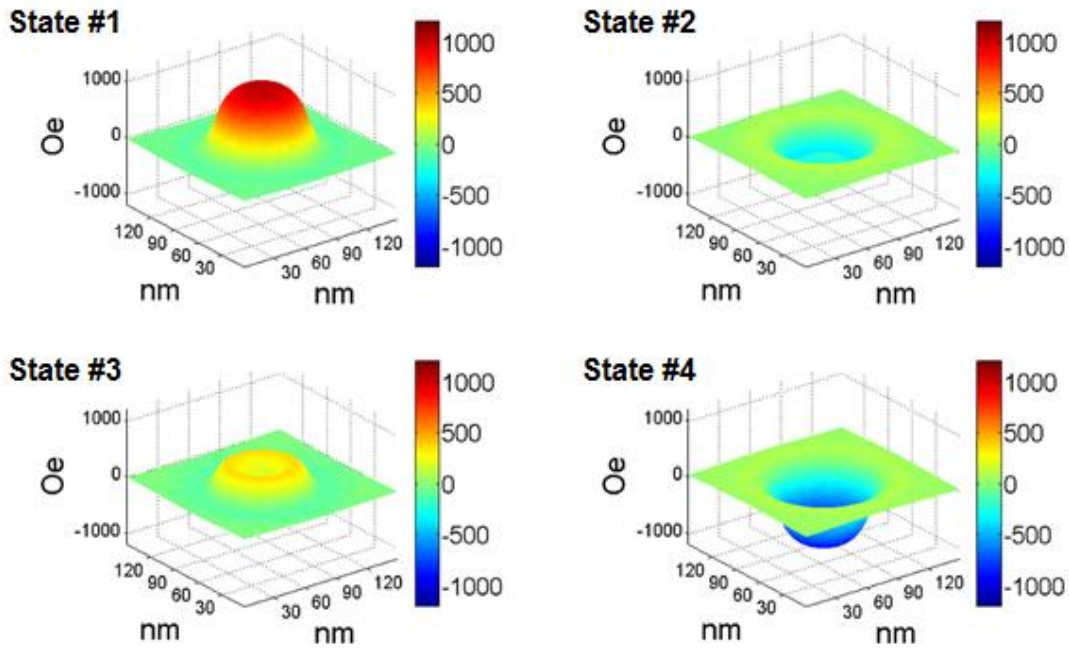

Figure 34: Four different states depends on magnetization directions of two cylinders

Chapter 5 Implementations of Perpendicular Multilayer MQCA

Two multiplayer MQCA devices (high density magnetic memory and magnetic majority gates) were developed as applications based on previous simulations demonstrated above. These devices share the fundamental idea that of being fabricated with materials with perpendicular (out-of-plane) crystalline anisotropy, and have similar three-dimensional architecture, which varies a little depending on scenarios.

Experimental Facilities

The experimental work includes two main aspects: fabrication and measurement. Fabrication approaches used include sputtering, electron beam lithography and focus ion-beam milling. All sputtering tasks were accomplished with an AJA Orion 5 sputtering system. As shown in Figure 35a, Ar ions hit the target surface. Atoms ejected from the target and distributed in the main chamber [59,60,61]. Collisions with the gas atoms that acts as a moderator and move diffusively, reaching the substrate to form thin films.

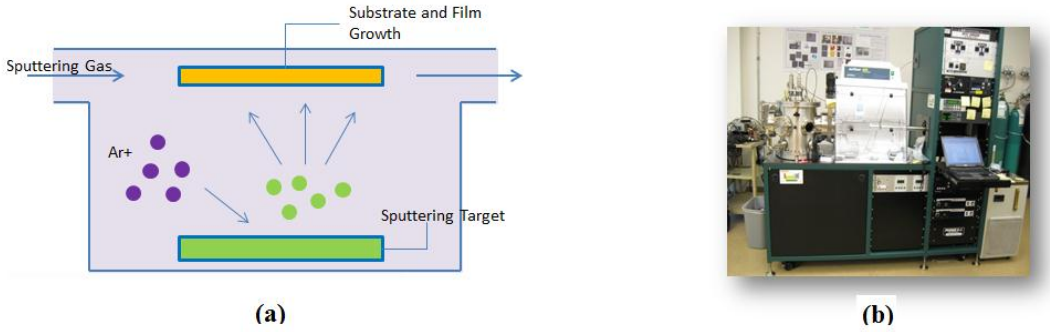

Figure 35: (a) Configuration of sputter deposition; (b) An AJA Orion 5 sputtering system in our laboratory

Electron Beam Lithography is used to fabricate periodic patterns. During this process, regions on a thin film, which is referred as “resist”, are selectively removed under a beam of electrons [62,63,64]. A JEOL direct-write JBX-5500FS EBL system was the main tool to crate ultra-small nano-scale structures for our experiments. Nanopatterns of ~10nm linewidth can be reached.

The magnetic hysteresis loops were measured by recording the polar signal with a Focused Magneto-Optical Kerr Effect system (F-MOKE system, Figure 36b). This is grounded on a phenomenon that reflected light from a magnetized surface will change its polarization and reflectivity. Based on the angular between the incident light and magnetization, there are three different types (Figure 36a). The magnetic field is measured with a hall probe placed between the pole tips [65,66,67]. Our F-MOKE system has a focusing length less than 1 μm.

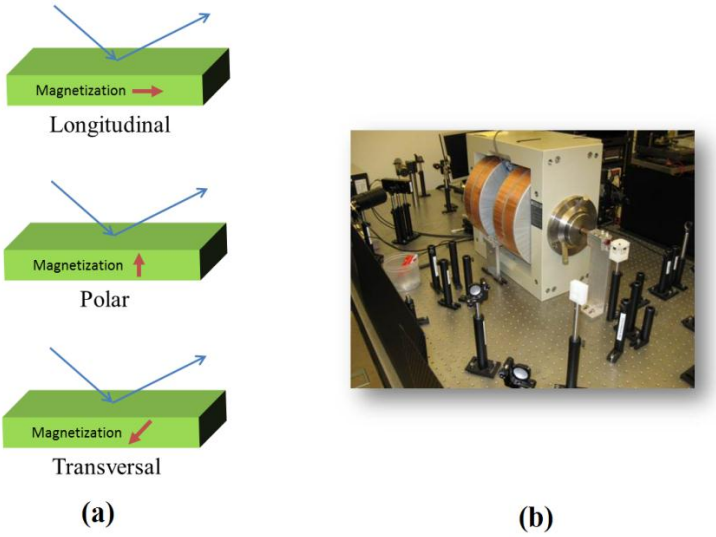

Figure 36: (a) Three types of Magneto Optical Kerr Effect measurements, classified according to the angle difference between incident light and magnetic material magnetization direction; (b) A picture of our MOKE system.

A scanning probe microscopy (SPM) system, Veeco Dimension 3000, was used to reveal and visualize the surface properties in nanoscale accuracy. It can serve as in either atomic force microscopy (AFM), or magnetic force microscopy (MFM) [68,69]. Figure 37a illustrates the schematic of MFM mode. A sharp magnetized tip scans the magnetic sample. During this process, the tip-sample magnetic interactions are detected and used to reconstruct the magnetic properties of the sample surface [70,71,72].

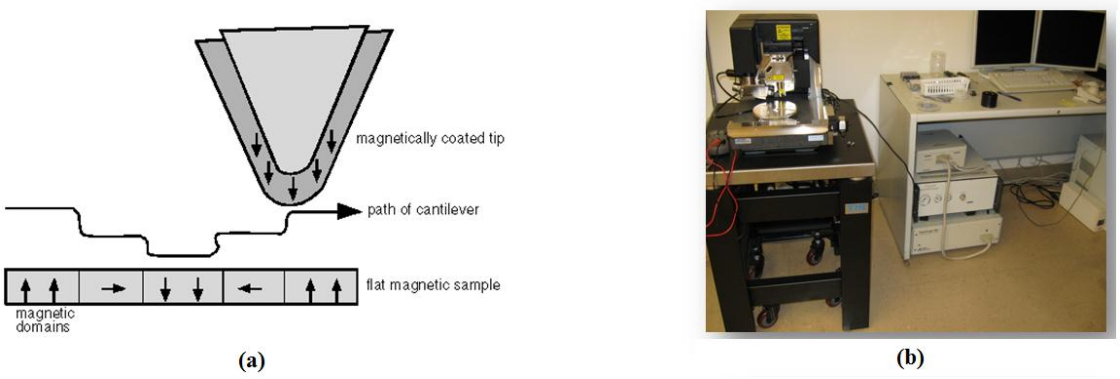

Figure 37: (a) MFM maps the magnetic domains of the sample surface; (b) A Veeco Dimension 3000 SPM system and corresponding computer for data processing.

High Density Magnetic Recording Device

The demand for magnetic memory of higher areal density always drives the industry and academia to develop novel storage technologies. Back in 2000, traditional longitudinal magnetic recording systems of areal density about 200 Gigabit/in^2 have already reached the superparamagnetic limit [73,74]. Afterwards, perpendicular magnetic recording technology that makes better use of disk real estate has gain the dominant position in hard drive manufacturing. Before reaching its superparamagnetic limit, perpendicular

recording is predicted to be able to attain around areal density of 1 Tarabit/in^2 in the near future [75].

Heat assisted magnetic recording (HAMR) is considered as a prospect technology for advancing to next generation storage system. Besides magnetic effects, a HAMR storage device also uses heat energy to manipulate the magnetization directions within magnetic layer which generally has extremely high anisotropy energy [76,77]. However, additional heating appliance capable of providing sufficient energy significantly increased the whole complexity of the magnetic recording system and hence become the main technical barrier in implementing HAMR devices [78,79].

Here, a novel high density magnetic storage technology utilizing MQCA arrays is reported. Inspired by the three-dimensional architecture of perpendicular magnetic tunnel junction, using similar structure but more magnetic layers has the potential to present more levels of magnetic stable states [80]. As of now, magnetic recording system based on MQCA networks has increasingly gain attention by storage industry and research institutions [81,82,83,84]. The schematic of our triple stack multilayer magnetic storage device is displayed in Figure 38. Each layer generates two readable and distinguishable signal levels, therefore the effective areal density increases by a factor of N. To selectively write on N layers, the multilayer there-dimensional magnetic media must exhibit a variation in magnetic properties across its thickness. One option is to create a coercivity gradient, where individual magnetic layers are accessed by changing the

magnitude and direction of the write field. As shown in Figure 38, m_1 and Hc_1 are the total magnetic moment and coercivity of the bottommost layer.

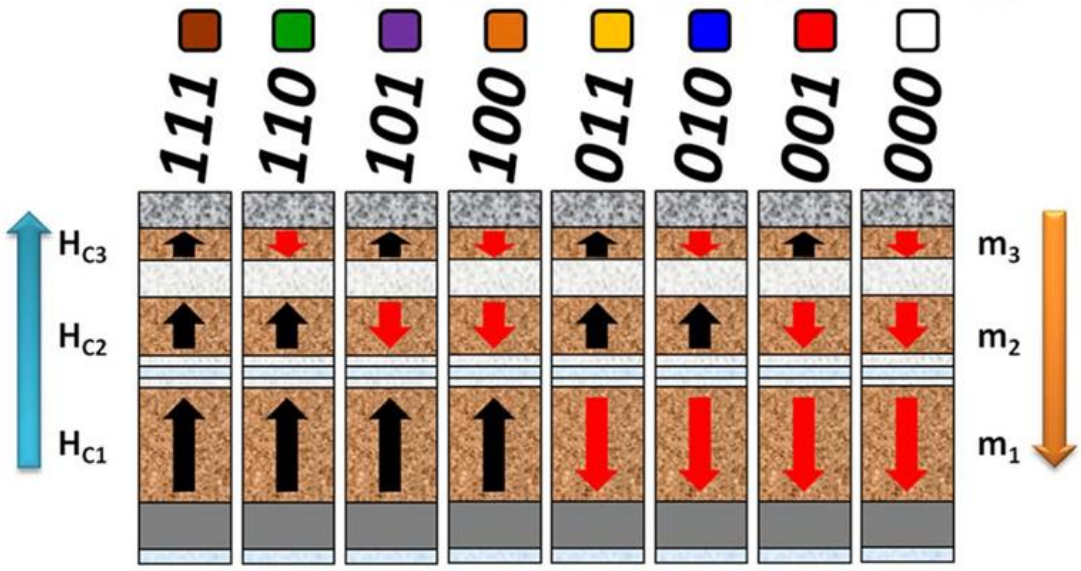

Figure 38: Magnetic media structure and preferred magnetic properties of each layer. Arrows of different color denote two stable magnetization directions, which are used to represent "0" and "1". Every possible combination is listed above the corresponding nanopillar.

Stacks of material with perpendicular anisotropy separated by isolation layers. The values of magnetization and coercivity of each layer has the following relationship: $m_1 \geq 2m_2 \geq 4m_3 \geq \ldots \geq 2^{N-1}m_N$ and $Hc_N > \ldots > Hc_3 > Hc_2 > Hc_1$. Co/Pt and Co/Pd have been proved to be the proper composition of the magnetic media [85,86].

Experimental Setup

In order to optimize the magnetic properties of silicon (Si 100) substrate supporting our magnetic media, Argon ion milling was done to the surface of SiO_2 before deposition. The complete recipe of our composition is (Silicon Substrate)/Ti(1.5nm)/Pt(5nm)/ [Co(0.4nm)/Pt(0.55nm)]×14/Pt(1.5nm)/Ti(1.5nm)/Pd(1.5nm)/[Co(0.25nm)/Pd(0.55nm)]×

7/Pd(4.5nm)/ [Co(0.25nm)/Pd(0.55nm)]×3/ Pd(3nm)/ Ti(4nm), illustrated by Figure 39. These thin layers were deposited with our ATA Orion 5 sputtering system described earlier. The titanium layer above the silicon substrate served as the hard-mask for the later pattern fabrication. Meanwhile, it was also an hydrogen silsesquioxane (HSQ) adhesion layer.

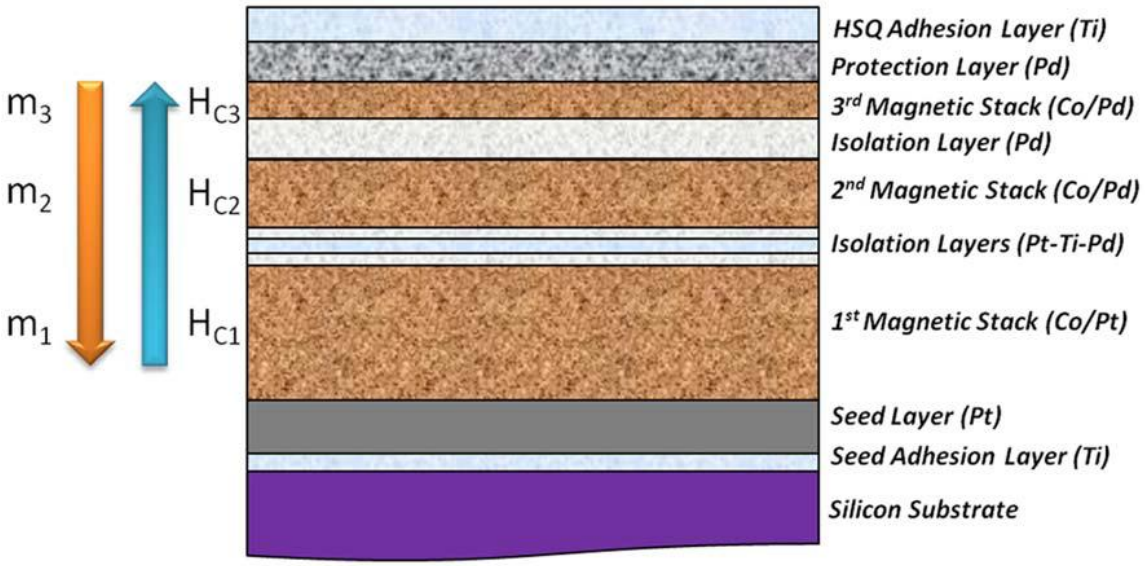

Figure 39: Complete configuration of magnetic media and silicon substrate. The magnetic media was placed on a silicon substrate.

Artificial patterns in nanoscale were fabricated through Electron-beam lithography (EBL). Primitive recording units, which on the whole are a set of periodic arrays of nanopillars, were carved out on the composition surface. The full fabrication processes are illustrated by Figure 40. First, an additional layer of HSQ and Methyl isobutyl ketone (mixture of 1:2.5) was spin-coated on top of the magnetic multilayers, and then processed by a 140 °C heat treatment. Afterwards, through JEOL JBX-5500FS direct-write EBL system, the sample was exposed to electron beam of 50 keV intensity, 98 pA current, and a dose

of 3000 μC/cm^2 on average. Eventually, a MICROPOSIT MF CD-26 solution was used to uncover the HSQ patterns exposed by the EBL system. Prior to the measurement step, generated nanopilars were examined by SEM and AFM to assure proper morphology and height.

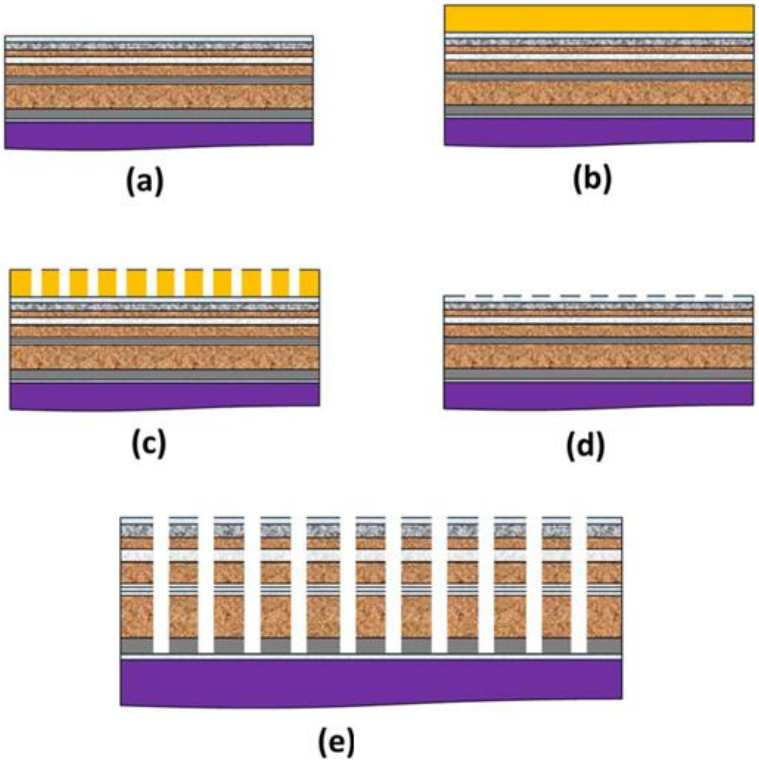

Figure 40: Pattern fabrication process. (a) Sputter-deposition of the triple-stack ML-3D magnetic media composition (b) Spin-coat and bake HSQ (c) E-beam lithography (expose and develop patterns) (d) ICP etching of the naturally oxidized Ti layer (e) Ar-ion milling of the remaining composition

Results and Discussion

Signal writing was performed through a saturate-reverse process by applying an external magnetic field. Desired intense of the external field was obtained based on the values of hysteresis loop measured by K-MOKE. As shown in Figure 41, six signal levels, 000,

001, 011, 100, 110, and 111, can be attained in two steps (saturate-reverse). The rest two signal levels need an additional step based on minor hysteresis loops.

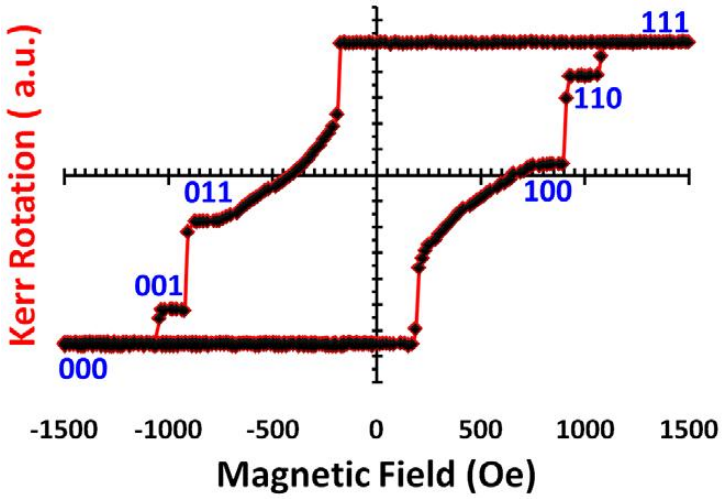

Figure 41: Hysteresis loop for the fabricated multilayer three-dimensional media

Signal reading was accomplished with MOKE measurement directly. First, a sequence of magnetic fields was applied externally to the magnetic media (Figure 42a). As a consequence of these external fields, the Kerr rotations produced by the multilayer magnetic media were recorded (Figure 42b). Depending on the

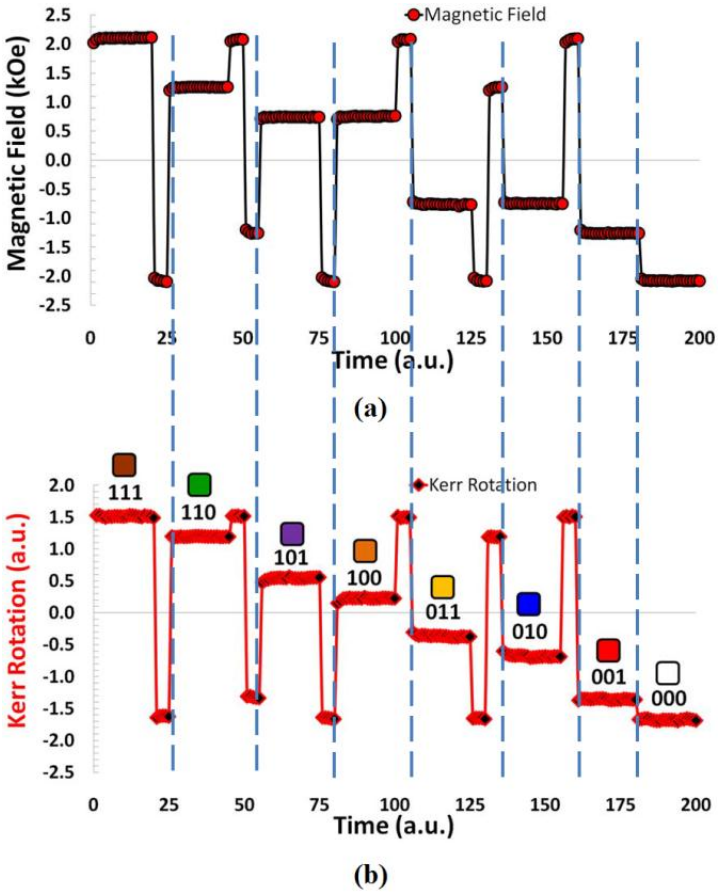

Figure 42: The simultaneous Kerr rotation produced by the ML-3D media as a result of the externally applied magnetic fields. Eight magnetic states can be distinguished.

To further study the feasibility of our perpendicular magnetic storage configuration, nanopillars in different areal densities were fabricated. Below the AFM and MFM images are presented (Figure 43). The brightness of a nanocell indicates its magnetization strength detected by MFM, which denotes corresponding magnetic signal level. “111” is the darkest, “000” is the brightest.

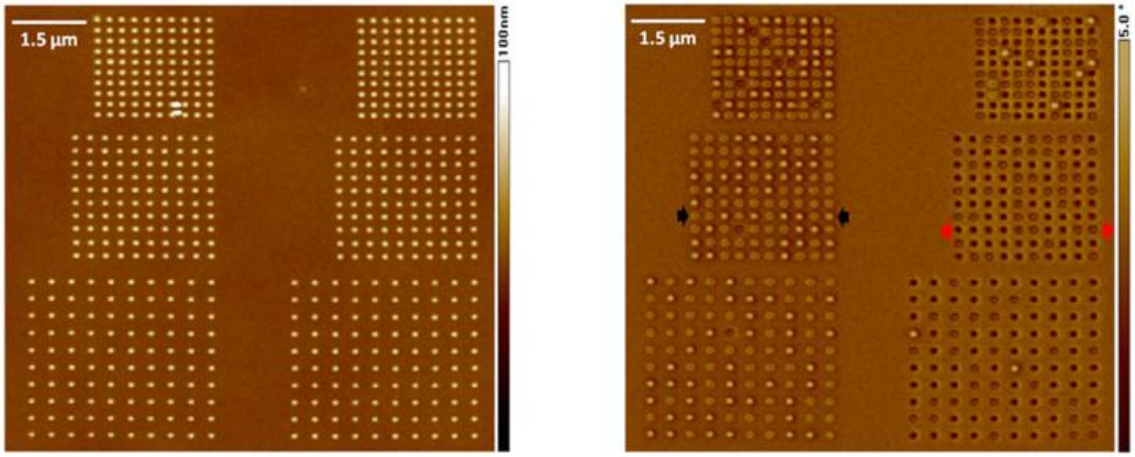

Figure 43: AFM(left) and MFM(right) images of perpendicular MQCA storage elements in different areal densities.

A more visual-friendly express of the signal levels is illustrated in Figure 44. Each magnetic state was assigned a unique color coding. The results proves that eight different signal levels can be distinguished, which proves the feasibility of applying our configuration to form high density magnetic recording system.

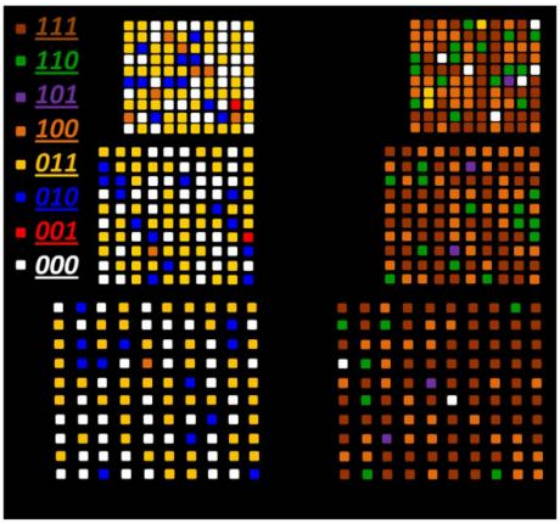

Figure 44: Color coding of nanocell magnetic states based on the data collected by MFM

It is worth to be noticed that nanocells in partially antiferromagnetic state were also stable. Partially antiferromagnetic state refers to those nanocells with magnetizations in different layers partially antiferromagnetically coupled, like “110” or “100”.

Further Extension: Universal Logic Gates

This is the three-dimensional architecture of majority logic gates implemented by multilayer MQCA networks (Figure 45). The “Up” and “down” magnetization directions denote bits “1” and “0, respectively. There are four layers of magnetic materials forming a reconfigurable gate implementation. Magnetic state of the output layer is determined by other layers.

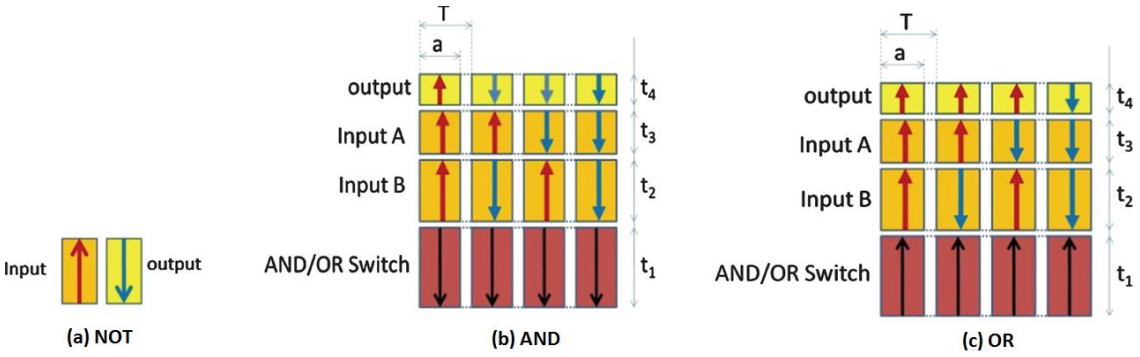

Figure 45: Modes of a four-layer reconfigurable gate implementation. (a) NOT; (b)AND; and (c) OR gate.

Similar to the three-layer magnetic recording unit, magnetic logic gates also formed by layers with perpendicular anisotropy energy separated by barrier layers. Recent studies of using Co/Pd multilayers for three-dimensional nanomagnetic logic devices have been presented [87]. In Figure 45a, two antiferromagnetically coupled adjacent cells to

represent an inverter, NOT. AND and OR gates have identical structure, depending on the magnetization orientation of the switching layer. Relationships between magnetic moment and coercivity values in four magnetic layers are: $m_4 = 2m_3 = 4m_2 = 8m_1$, $Hc_4 > Hc_3 > Hc_2 > Hc_1$. The optimized locally averaged values of the magnetization of the four magnetic layers were approximately 425, 305, 180, and 115 emu/cc, respectively from bottom to top. Meanwhile, the desired coercivities of each layer were 3.2, 2.4, 1.1, and 0.5 kOe, respectively.

Due to the distinct magnetization of each layer, AND and OR Boolean functions can be obtained (Table 2). As for the NOT gate, it can be implemented simply through two antiferromagnetcally coupled nanocells.

Input A	1	1	0	0
Input B	1	0	1	0
AND Output (Switch = 0)	1	0	0	0
OR Output (Switch = 1)	1	1	1	0

Table 2: The truth table of our four-layer magnetic logic gates (AND & OR).

Experimental Setup

AJA Orion 5 sputtering system was used to deposit Co/Pd multilayer films on a glass substrate. The base pressure for all samples was set to below 1×10^{-7} Torr. An Ar+ milling was implemented to the substrates through RF substrate biasing before the deposition. This process lasted for around two minutes, for a power of 25W and a pressure of 5 mTorr. Target holder with in the sputtering chamber was rotated at a rate of 40 rpm, in

order to attain uniform deposition. Processing pressure of 5 mTorr was set to deposit the Pd seed and capping layers. The seed layer is the one at the bottom (Figure 46). As for the Co/Pd bilayers, the pressure was set to 15 mTorr. Deposition rate for the Pd seed and capping layers were 0.43 Å/s, and 0.35 and 0.63 Å/s for the Co and Pd layers, respectively.

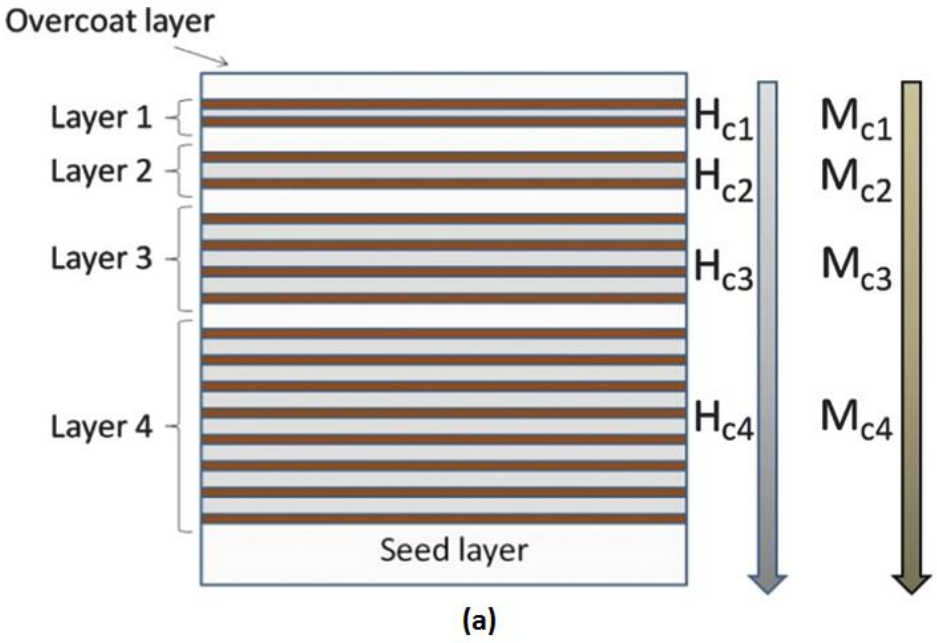

Figure 46: A not to scale schematic of our four-layer magnetic logic gates configuration. Layer with higher magnetization contains more Co/Pd thin film pairs.

Results and Discussion

The focused MOKE system was used to measure the hysteresis loop (Figure 47) of our magnetic AND/OR gate. Minor loops are shown by different colors. On shoulders of the loop, magnetic states of the four layers were coded as AND/OR switch, input B, input A, and output.

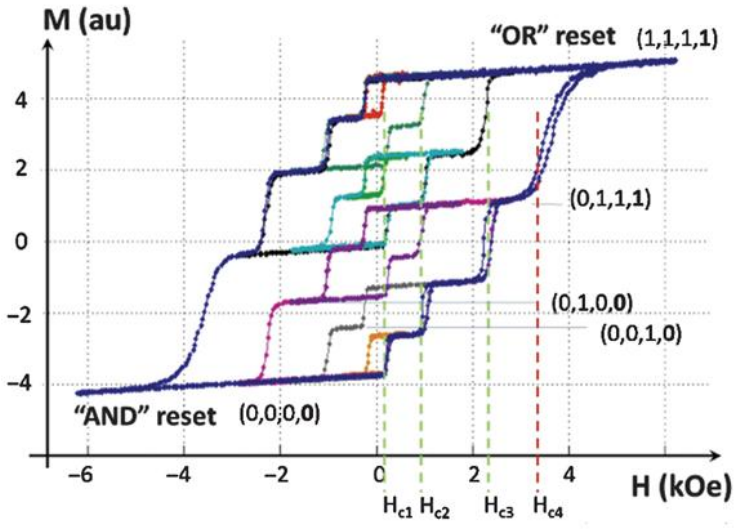

Figure 47: Complete M–H hysteresis loop measured by focused MOKE system. Stable magnetic states were attained for different combinations of input and switching setup.

For MFM imaging study, a slight modification was made to the multilayer magnetic AND/OR gate. Because MFM probe interaction effect is too large for the four-layer architecture, another three-layer structure was fabricated (Figure 49). Although with the architecture simplified, our experiments still gave some insight into the physics of the operation of 3D logic gates.

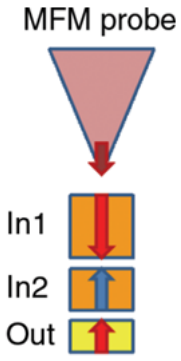

Figure 48: The simplified three-layer nanopillar used in MFM imaging.

The AFM and MFM images are shown in Figure 49. Brightness of a nanomagnet shows the net magnetic field detected by MFM (darkest ones were “000” and brightest ones were “111”). Each dot was of 80 nanometer diameter.

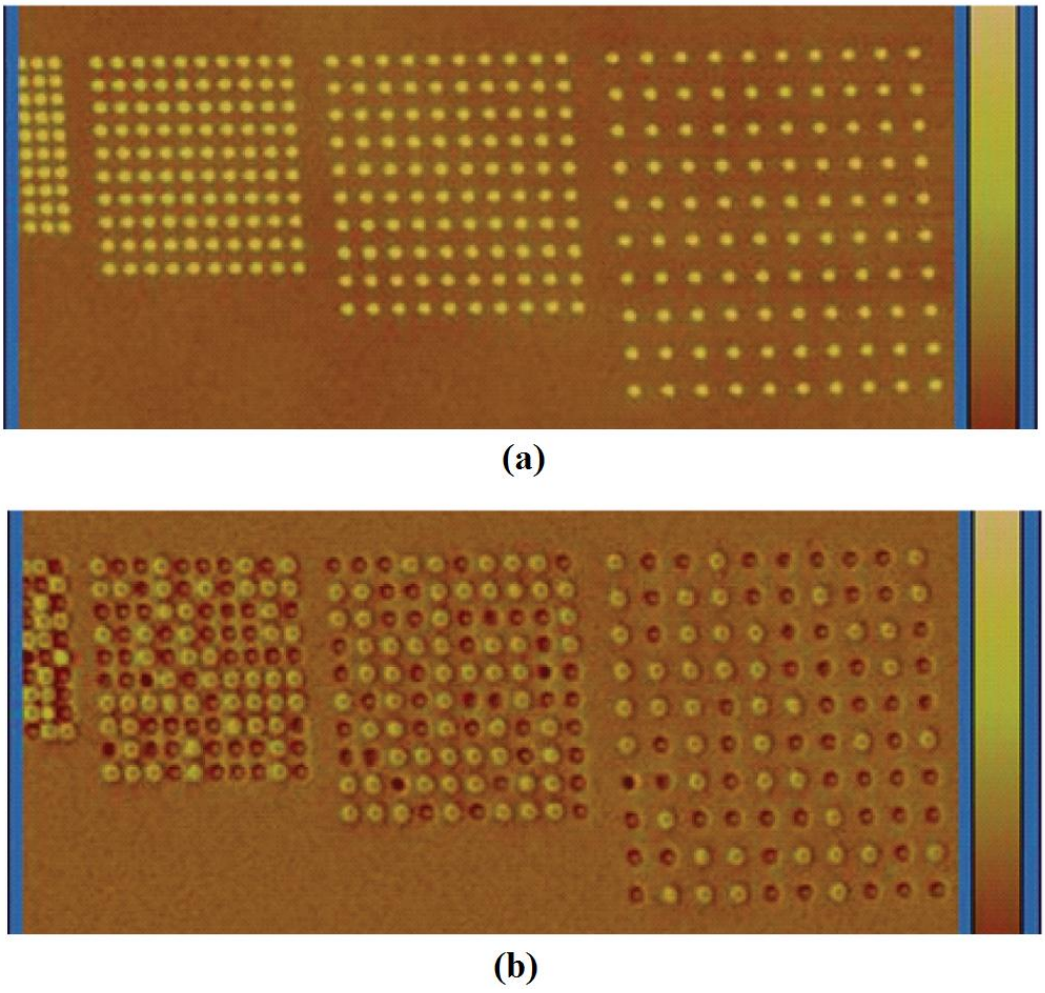

Figure 49: (a) AFM and (b) MFM images of three-layer magnetic logic elements in different areal densities.

To study the stability of each magnetic state determined by magnetization of each layer, a gradually varied magnetic field was applied externally to all samples. The MFM measurement was done after removing this field. As shown in Figure 50, in the beginning

the external magnetic field was sufficiently large (-0.5 Tesla) to saturate both input layers to be "1". Then with time changes, the external field was reversed to be +0.2 Tesla, which was not able to switch the magnetization of the upper layer (Input 1), but enough to reverse the middle one (Input 2). Similar but in opposite direction, the input layers changed their magnetization according to external field of +0.5 and -0.2 Tesla (the latter two images of Figure 50). In all four cases, the output layer presented desired magnetization direction determined by the inputs.

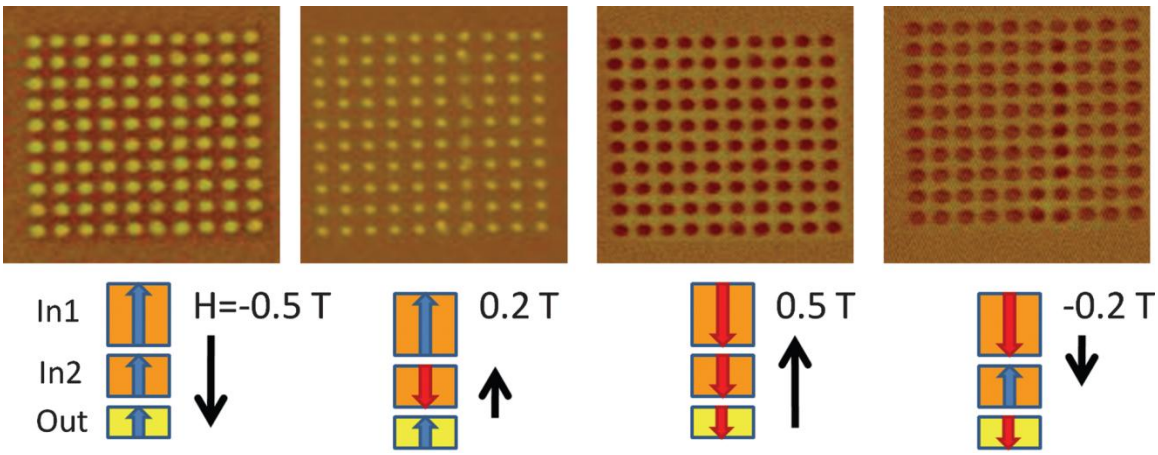

Figure 50: MFM images shows the brightness change according to the external magnetic field varying with time.

In summary, significant progress substantiating the feasibility of using four-stack multilayer MQCA as AND and OR logic gates was demonstrated. Benefits from the unequal magnetization in each magnetic thin film, multilayer MQCA with perpendicular anisotropy energy is proven to have possibility to be used in other scenarios other than in recording system.

Chapter 6 Energy-efficient Spin-transfer Torque Magnetic Tunnel Junction Magnetization Reversal

Spin Transfer Torque (STT) Magnetic Tunneling Junction has many merits: high density, high speed, non-volatile, low static power consumption [88 , 89 , 90]. Spin-transfer torque is an effect in which the orientation of a magnetic layer in a magnetic tunnel junction or spin valve can be modified using a spin-polarized current [91]. This phenomenon is based on the truth that the angular momentum of a spin-polarized (switching) current can be transferred.

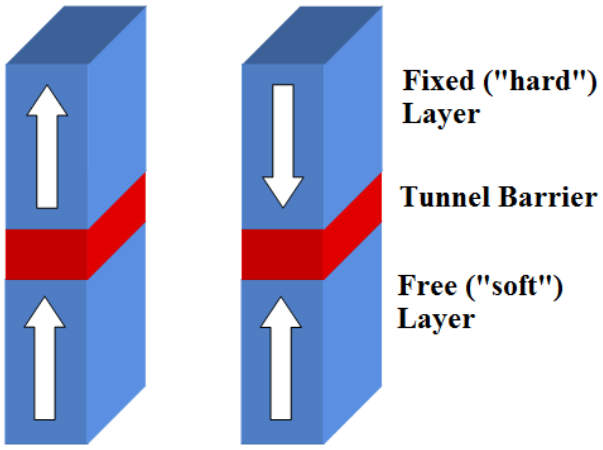

Figure 51: Magnetic tunnel junctions with perpendicular anisotropy: (left) parallel magnetization state and (right) anti-parallel magnetization state.

The principle difficulty in the implementation of STT MTJ is how to reduce the required switching current. Heat-assisted switching has been studied to lower the current needed, but it brings other extra drawbacks, like more complicated structure and additional power consumption. An alternative approach is to shrink the size of MTJ. Several essential

achievements have been reported in this field: 3.9 MA/cm2 for a 40-nmcell by S. Ikeda et al [92]; 9.2 MA/cm2 for a 20-nmcell by M. Gajek et al. [93], and more than 290 MA/cm2 for a 100-nm cell by R. Sbia et al. [94].

In this section, STT MTJ with cross-sectional dimensions in sub-10nm was reported. Such MTJ can significantly reduce switching needed current compared to other approaches, much better than merely due to the scaling effect. This is because of the extremely small energy absorbed by thermal reservoir and less effective energy exchange between excitations in sub-10nm region [95]. Before experimental work, a numerical model was simulated to consolidate our theory.

Simulation

Based on atomistic-scale quantum-mechanical principles, numerical simulations of the spin excitations were performed for two cubic devices with side length of 15nm (top row) and 2nm (bottom row) [96]. All spins were aligned completely in the Z-direction in the initial state. An external magnetic field, H_z, was applied when simulation began. The modeling results were revealed in Figure 52. As can be seen, in the sub-10nm region, spins have much slower relaxation and stronger spin-spin coherence, compared to spins in the above-10-nm range. Plus, the damping effect in the sub-10-nm range was significantly reduced to almost negligible.

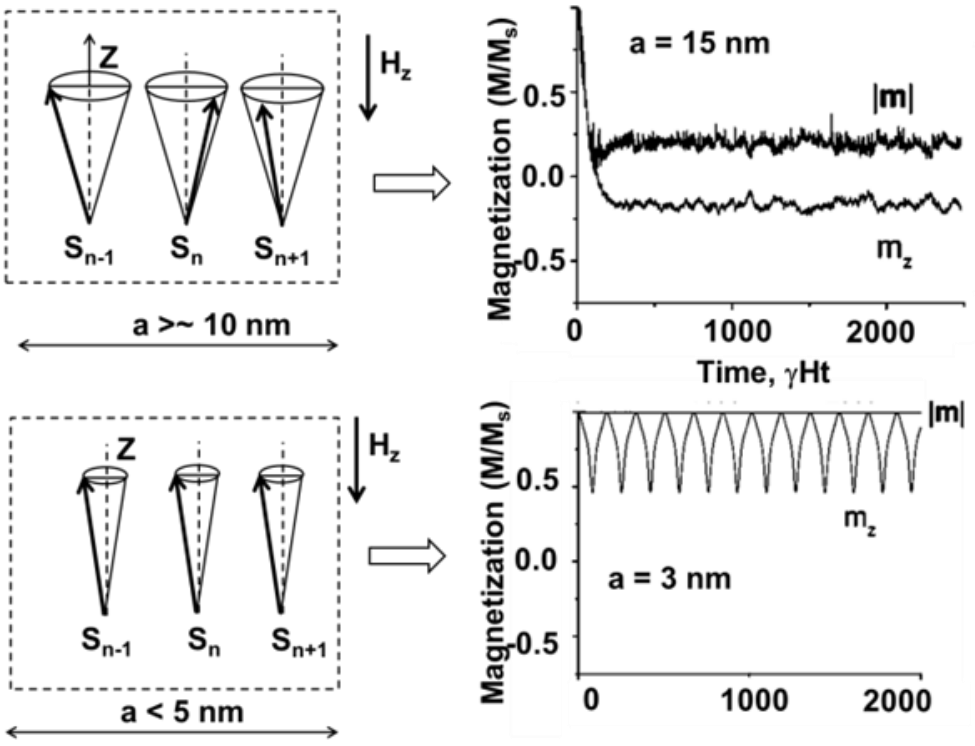

Figure 52: Simulation results of the spin relaxation process in two regions of interest. (i) above-10-nm range (top row) and (ii) sub-10-nm range (bottom row).

The simulation results sustained our hypothesis and motivated further experimental work. When devices are miniaturized to sub-10-nm region, the change in spin relaxation is not affected merely by the linear scaling effect.

Experimental Setup

CoFeB/Mgo/CoFeB junction has been proved to have large TMR effect ratio [97], which is desired in distinguishing two MTJ states of different electrical resistance. Besides, it is considered to be able to provide high spin torque efficiency and ultra-high perpendicular anisotropy. Therefore, Ta(5nm)/CoFeB(1nm)/MgO(0.9nm)/CoFeB(1nm)/Ta(5nm), was chosen to be the perpendicular multilayer composition of our MTJ. The titanium layers served as contact of the magnetic tunnel junction. After being sharpened by focused ion

beam (FIB), a scanning tunneling microscopy (STM) probe was coated with the multilayer composition through spattering deposition (Figure 53a).

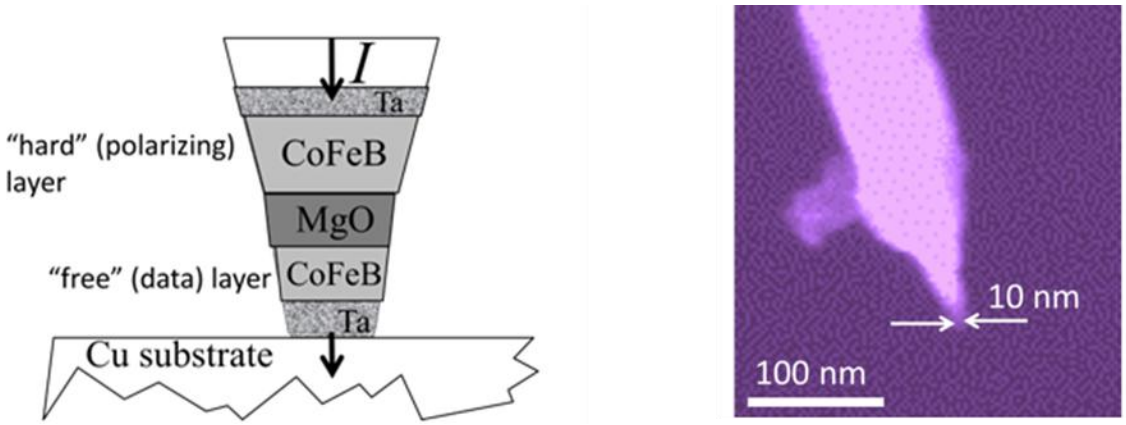

Figure 53: (left) An exaggerated illustration of a MTJ coated with a thin Ta layer on the top of a STM probe; (right) A SEM image of a nanoprobe with a MTJ coated on the tip.

The last layer in the probe tip is the "free" magnetic layer while the other one is the "fixed" layer. The extremely small MTJ cross-section with point contact was reached between the STM probe and the copper substrate. In this region, energy barrier introduced by the perpendicular anisotropy is sufficient to match the requirement of thermal stability ($>20\ K_uV/k_bT$). Through adjusting the mechanical pressure between the coated STM probe and the copper substrate, robust resistance can be reached from 30 kOhm to 200 kOhm.

Results and Discussion

The differential resistance is the changing rate from high resistance status to low resistance states of a magnetic tunnel junction. It is also called tunneling magneto-resistance (TMR) effect and defined by the equation below:

$$\text{TMR effect ratio} = \frac{R_{ap} - R_p}{R_p} = \frac{\Delta R}{R}$$

R_{AP} and R_P are the resistance in antiparallel and parallel aligned magnetizations, respectively. It indicates the difference between two states due to TMR effect.

Figure 54 shows the hysteresis loop of differential resistance (ΔR/R) versus current measured by MOKE system. The average contact resistance was 185 kOhm. It can be seen that the reversal current to switch the MTJ from antiparallel state to parallel state (I_{AP-P}) was 0.06μA, and the current switching the MTJ from parallel state to antiparallel state (I_{P-AP}) was 0.13μA. Therefore, the average spin reversal current will be the (0.06 + 0.13)/2 = 0.095μA (95nA). The TMR effect ratio was approximately 29%.

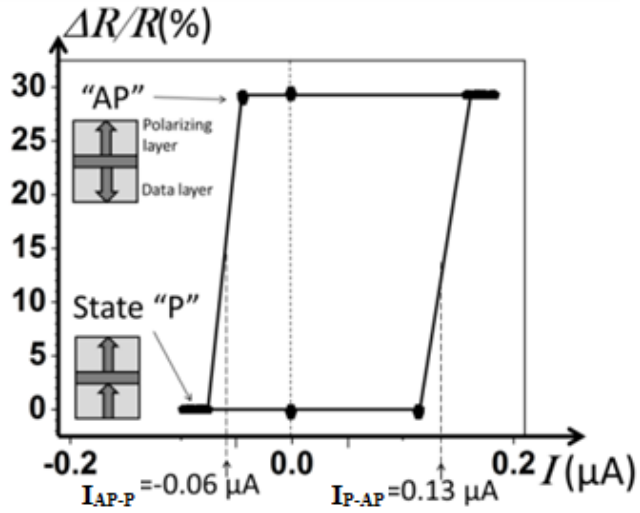

Figure 54: Hysteresis curve of TMR effect amplitude versus current for a point contact MTJ with an average resistance of 185 kOhm.

An external magnetic field can help reduce the required switching current. As shown in Figure 55a, the average switching current (I_{SW}) is lowered along with the increase of the

magnetic field (H_0). Figure 55b shows the in-plane and out-of-plane hysteresis loop recorded by focus MOKE system.

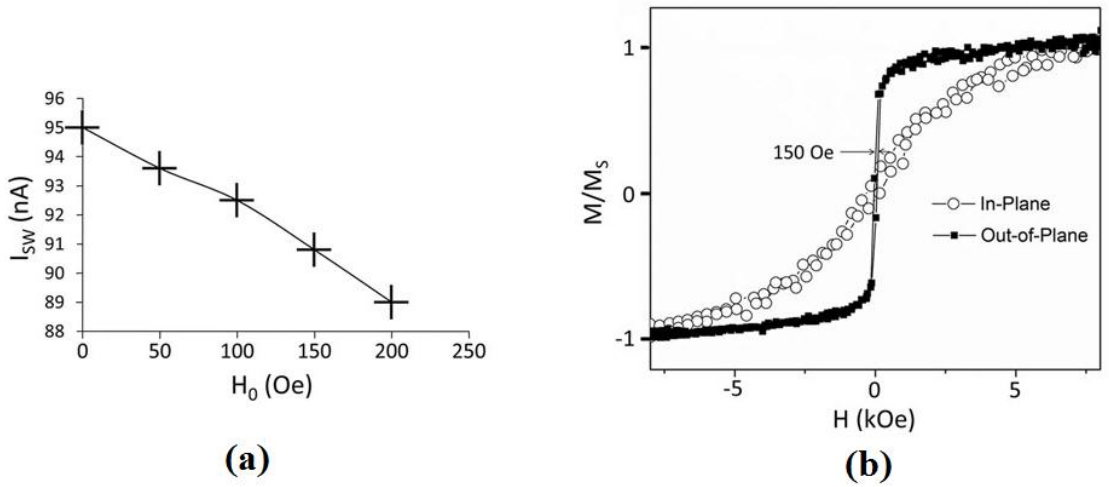

Figure 55: (a) Switching current lowered as the increasing of an external magnetic field. (b) M-H hysteresis loop of in-plane and out-of-plane measured by focus MOKE system.

According to previous report of the average switching current (49μA) of a 40nm scale magnetic tunnel junction, the projected average switching current of a 10nm MTJ is about 3μA. Compared to this value, our result (95nA) is approximately 30 times smaller. Based on Slonczewski's theory [98], a simple phenomenological estimation of the switching current density can be gain:

$$J_{AP-P} = AM_s t \frac{\alpha}{p\xi}\left(H_{eff} \pm H_0\right)$$

Here A is the model constant, H_{eff} is the effective anisotropy field including both intrinsic and shape anisotropy, H_0 is the external field used to reduce the switching current effectively, α is the damping constant, p is the spin polarization (the value of p is 0.36

based on Julliere's expression [51], R/R = $2p^2/(1-p^2)$ for □R/R ≈ 29% assuming the magnetoresistance was mostly initiated by the MTJ core), ξ is the spin torque efficiency factor, Ms is the saturation magnetization (500 emu/cc), and t is the thickness of the "free" layer (1nm).

In order to further understand the magnetic properties of STT MTJ in sub-10-nm region, repeated experiments were done for various contact resistances. By adjusting an Angstrom-precision control in the vertical direction, resistance can be changed from approximately 30kOhm to 200kOhm. Differ from traditional point contact of a MTJ, our contact is between the tip of a probe and the Cu substrate. 26 kOhm, 95 kOhm, and 185 kOhm were selected for our study. Figure 56 shows their resistance-current and TMR effect ratio-switching current hysteresis curves. It is worth to be noticed that the value of average switching current for the three wild-spread contact resistances barely changed (Figure 56b).

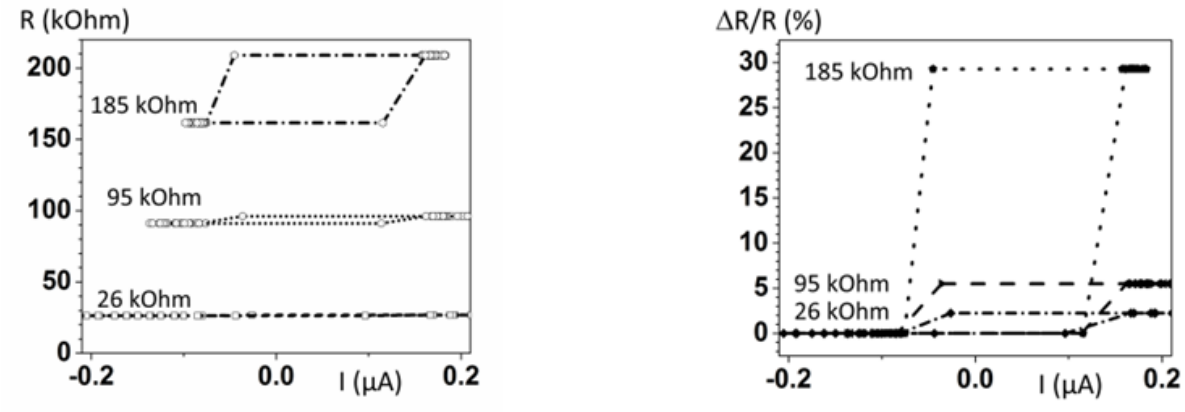

Figure 56: (a) Resistance-current hysteresis curves for three samples having different contact resistance of 26, 95, and 185 kOhm; (b) TMR effect ratio versus switching current for the same three cases.

In conclusion, the average switching current measured in our experiments of magnetic tunnel junction of size in sub-10nm region was around 100nA, which is at least an order of magnitude less than previous reported value. This dramatically lowered switching current is of great important significance for MRAM industry. In additional, the irrelevance between contact resistance and average switching current was also reported.

Chapter 7 Future Research

Optimization of Signal Propagation Speed in MQCA Channels

The speed of signal propagation is always an important issue in an information transfer system. Nanomagnets, or nanomagnetic cells, are the most elementary units of a MQCA network. Broadly speaking, the easier to switch a nanocell, the faster to propagate signal in a MQCA data channel. Nanocells composed by material with larger anisotropy energy are more likely to switch. But in the other hand, every nanocell trend to align their magnetization direction to its easy axis. Therefore high anisotropy will also reduce the stability of nanomagnets saturated to their hard axis and leads to misalignments. Thus, there is a tradeoff between speed and reliability. In addition, as shown earlier in Figure 18, signal propagation distance has also had an inverse relationship with nanomagnets reliability.

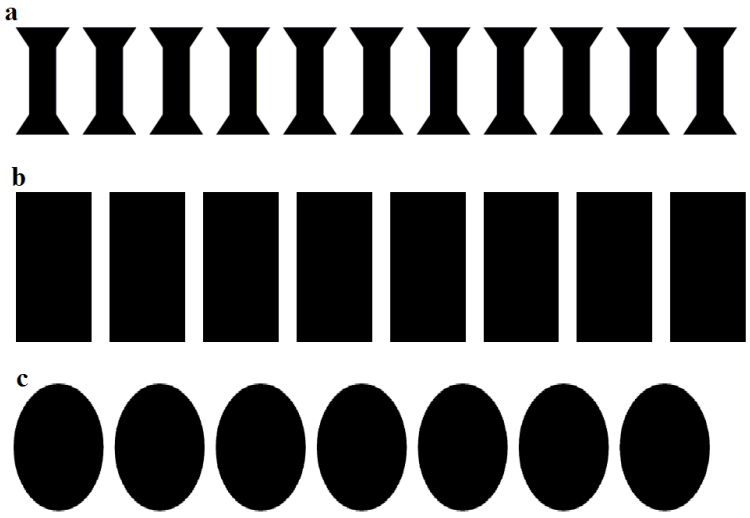

Figure 57: MQCA data channels composed of nanomagnetic cells with different shapes (a) Pillar; (b) Rectangular; (c) Oval.

The investigation for finding a compromise for signal propagation speed, range, and reliability is an interesting issue. By changing the spacing, anisotropy energy, and the amplitude of holding field and clocking field, the optimized structure can be found. Furthermore, various materials will be tested, since intrinsic magnetic properties like saturation magnetization, exchange energy, etc. can also affect the speed and reliability.

Figure 57 shows MQCA data channels composed of nanocells with shape of pillar, rectangular, and oval. Fabrication of nanocells in a certain shape is not trivial as modeling. To cooperate with fabrication in reality, it is necessary to study the effect brought by imperfect shape of nanocells.

Figure 58: Simulation of initiating input signal by another MQCA data channel. Cell a is the last nanocell of another MQCA wire.

Magnetic signal coupling is also an essential issue. In previous simulations, the input signal was set to either “0” or “1” directly, by initiating the magnetization of the first nanocell to its easy axis. However in reality, the input signal shall be served from other MQCA data channel in a far less ideal way. The magnetic spray field generated by components in this data channel will eventually affect the input signal coupling. Figure 58 shows a simulation of initiating the input cell (cell B) of a MQCA data channel by utilizing the spray field of another nanocell A.

Addressing Challenges of Implementing Multilayer MQCA Networks

Although multilayer MQCA networks built by material with perpendicular anisotropy has been proved to be feasible in composing high density magnetic recording and majority logic gate devices, some challenges remain to be investigated.

First, how to continually increase the number of magnetic thin films in multilayer magnetic recording device is worth to be studied. More magnetic layers indicate more levels of signals can be stored. However, fabrication and signal processing also become harder. Applying a varying external magnetic field indeed can have a multilayer recording unit reach desired state, but in reality this external field can hardly be scaling down to nanoscale. In addition, as a consequence of higher information density, distinguishing magnetic signal becomes more difficult. Many interesting problems remain in this field.

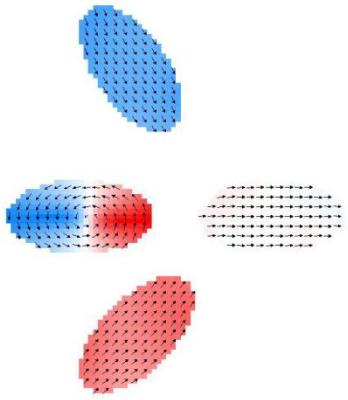

Figure 59: Model of a magnetic majority gate with oval shape MQCA nanocells. Nanocells were tilted to adjusting magnetic coupling effects.

Another issue for using multilayer MQCA for logic devices is how to selectively change the magnetization of a particular layer. The inputs of a logic gate shall be changeable

freely. Approaches to realize proper signal coupling in nanomagnet majority gates is still an open question. Shape anisotropy and crystalline anisotropy are not mutually exclusive and may contribute together for novel MQCA architectures. Figure 59 shows a developing majority gate model. In this configuration, oval nanomagnets are used to form the MQCA network. The variation of magnetic coupling effect regarding to the changing tilted angles of two input pads are being investigated.

Conclusion

In summary, key technical obstacles faced by silicon-based semiconductor industry were reviewed. As a promising alternative for next generation information storage and computing architecture, magnetic logic systems, especially magnetic quantum-dot automata system were introduced. Micromagnetism studies were demonstrated.

Feasibility of using crystalline (instead of shape-induced) magnetic anisotropy to build patterned nanomagnetic data channels is demonstrated. Both in-plane and out-of-plane anisotropy cases are studied. The results indicated that using new cost-effective magnetic structures indeed could provide substantially greater flexibility in the design of a magnetic channel. Such flexibility is crucial in the design of ultra-high density and ultra-fast non-volatile magnetic logic devices. Through numerical simulations, design trade-offs is found to be necessary for optimizing important technical characteristics of magnetic logic, such as packing densities, data rates, and stability and reliability. The expansibility to 3D logic devices by using nanocells with out-of-plane anisotropy is demonstrated.

Simulations for a perpendicular magnetic tunnel junction were presented. Modeling results shown our MTJ configuration is capable of obtain stable and distinguishable magnetic states according to all four possible magnetization combinations of the two magnetic layers.

Besides, two implementations of multilayer nanomagnetic networks composed with materials with out-of-plane crystalline anisotropy, universal logic gates and high density magnetic signal memory are explored in both simulation and fabrication. Experimental

results further confirmed the positive prospect of three-dimensional multilayer nanomagnetic logic devices. Approaches to write and record expected stable and distinguishable magnetic states are provided.

In the last section, an energy-efficient spin-transfer torque (STT) reversal in magnetic tunnel junction (MTJ) of sub-10nm was explored. Numerical simulations revealed that the energy required to reverse magnetization is significantly superior to effect due to scaling down of the size. Experimental work shows the switching current of device in sub-10nm region is at least an order of magnitude less than previous reported value. Reducing the switching current requirement for STT MTJ directly leads to more power efficient MRAM, a significant improvement for magnetic memory industry.

Appendices

A. Symbols

B Magnetic induction

E: Energy

H: Magnetic field

Hc: Coercivity field

H$_{eff}$:Effective magnetic field

J: Dipolar coupling energy

k: Boltzmann's constant

K_1: Magneto-crystalline anisotropy

M_S: Saturation magnetization

p: Spin polarization

r: Spatial position

t: Time

T: Temperature

T_C: Curie temperature

α: Damping constant of the Landau-Lifshitz-Gilbert (LLG) equation

γ: Gyromagnetic ratio

ξ: Spin torque efficiency factor

B. Selected Publications and Presentations

- **Y. Tian**, L. Kaganovskiy, N. Amos, B. Hu, D. Litvinov, and S. Khizroev, "Effects of Crystalline Anisotropy on Nanomagnetic Computer Logic Channels," J. Nanoelectronics and Optoelectronics. 6, 87-94 (2011).

- **Y. Tian**, N. Amos, B. Hu, D. Litvinov, and S. Khizroev, "Consideration in the Design of Highly Scalable Magnetic Logic Channel," 55th MMM Conference, Atlanta, GA, Nov. 14-18, 2010.

- B. Hu, N. Amos, **Y. Tian**, D. Litvinov, and S. Khizroev, "Study of Co/Pd Multilayers as a Candidate Material for Next Generation Magnetic Media," J. Appl. Phys. 109, 034314 (2011).

- N. Amos, E. Stefanescu, J. Butler, B. Lee, **Y. Tian**, et al. "Three-Dimensional Non-Volatile Magnetic Universal Logic Gates," J. Nanoelectronics and Optoelectronics. 6 (2), 132-137 (2011).

- N. Amos, J. Butler, B. Lee, MH Shachar, B. Hu, **Y. Tian**, et al. "Multilevel-3D Bit Patterned Magnetic Media with 8 Signal Levels Per Nanocolumn", PloS one. 7(7), e40134 (2012).

Bibliography

[1] Moore, Gordon E. “Cramming more components onto integrated circuits.” Electronics Magazine. p. **4** (1965).

[2] Powell, James R. "The quantum limit to Moore's law." Proceedings of the IEEE **96.8**: 1247-1248 (2008).

[3] J. D. Mel, Q. Chen, and J. A. Davis. “Limits on Silicon Nanoelectronics for Terascale Integration. Science.” **293**, 2044 (2001).

[4] Rupp, Karl, and Siegfried Selberherr. “The economic limit to Moore's Law.” Semiconductor Manufacturing, IEEE Transactions on **24.1**: 1-4 (2011).

[5] F. Abouzeid, S. Clerc, F. Firmin, M. Renaudin, and G. Sicard. “A 45-nm CMOS 0.35v-Optimized Standard Cell Library for Ultra-low Power Applications.” Proceedings of the 14th ACM/IEEE Int. Symposium on Low-Power Electronics and Design, (2009).

[6] J. Yuan, J. D. Cressler, R. Krithivasan, T. Thrivikraman, M. H. Khater, D. C. Ahlgren, A. J. Joseph, and J. Rieh. “On the Performance Limits of Cryogenically-Operated SiGeHBTs and Its Relation to Scaling for TeraHertz Speeds.” IEEE Trans. on Electron Devices. **56 (5),** 1007 (2009).

[7] C. Hallmark. “THE END IS NEAR! For Moore's Law and Our 25-Year-Old Cyber-Finance Economy.”, http://www.indymedia.org.uk/en/2006/08/347233.html

[8] http://www.itrs.net/Links/2010ITRS/2010Update/ToPost/2010TablesORTC_ITRS.xls

[9] S. Borkar, T. Karnik, V. De. “Design and Reliability Challenges in Nanometer Technologies.” Proceedings of the 41st annual Design Automation Conference, (2004).

[10] R. P. Cowburn. “Where Have All The Transistors Gone.” Science. **311**, 183 (2006).

[11] N. Amos, R. Ikkawi, A. Krichevsky, R. Fernandez, E. Stefanescu, I. Dumer, D. Litvinov, and S. Khizroev. “Multilevel Three-Dimensional Nanomagnetic Recording.” J. Nanoelectron. Optoelectron. **2**, 257 (2007).

[12] U. F. Gianola. “Possibilities of All-Magnetic Logic.” J. Appl. Phys. **32**, 27 (1961).

[13] Prinz, G. A., and K. Hathaway. “Physics Today.” Spin-polarized Transport. **48**: 353-363 (1995).

[14] D. Bennion, H. Crane, and D. Nitzan, "Digital Magnetic Logic." McGraw-Hill, New York (1969).

[15] www.sri.com

[16] A. Imre, G. Csaba, L. Ji, A. Orlov, G. H. Bernstein, and W. Porod. "Majority Logic Gate for Magnetic Quantum-Dot Cellular Automate." Science. **311**, 205 (2006).

[17] D. A. Allwood, G. Xiong, M. D. Cooke, C. C. Faulkner, D. Atkinson, N. Vernier, and R. P. Cowburn, "Submicrometer Ferromagnetic NOT Gate and Shift Register." Science. **296(5575)**, 2003-6 (2002).

[18] M.C.B. Parish and M. Forshaw. "Physical Constraints on Magnetic Quantum Cellular Automata." Appl. Phys. Lett. **83**, 2046 (2003).

[19] Amlani, Islamshah, et al. "Digital logic gate using quantum-dot cellular automata." Science **284**.5412: 289-291 (1999).

[20] Orlov, A. O., et al. "Realization of a functional cell for quantum-dot cellular automata." Science **277**.5328: 928-930 (1997).

[21] A. Orlov, A. Imre, G. Csaba, L. Ji, W. Porod, and G. H. Bernstein. "Magnetic Quantum-Dot Cellular Automata: Recent Development and Prospects." J. Nanoelectron. Optoelectron. **3**, 1 (2008).

[22] R. P. Cowburn. "Probing Antiferromagnetic Coupling between Nanomagnets." Phys. Rev. B. **65**, 092409 (2002).

[23] C. Augustine, B. Behin-Aein, X. Fong, and K. Roy. "A Design Methodology and Device/Circuit/Architecture Compatible Simulation Framework for Low-Power Magnetic Quantum Cellular Automata Systems." Proceedings of the 2009 Asia and South Pacific Design Automation Conference, (2009).

[24] A. V. Jausovec, G. Xiong, and R. P. Cowburn. "Stability of Magnetization States in Submicron Permalloy Disks." J. Appl. Phys. **99**, 08B103 (2006).

[25] Y. Tian, L. Kaganovskiy, N. Amos, B. Hu, D. Litvinov, and S. Khizroev. "Effects of Crystalline Anisotropy on Nanomagnetic Computer Logic Channels." J. Nanoelectronics and Optoelectronics. **6**, 87-94 (2011).

[26] D. Weller and A. Moser. "Thermal Effect Limits in Ultrahigh-Density Magnetic Recording." IEEE Trans. Magn. **35**, 4423 (1999).

[27] R. P. Cowburn and M. E. Welland. “Room-Temperature Magnetic Quantum Cellular Automata.” Science. **287**, 1466 (2000).

[28] A. Imre, Ph.D. Thesis. “Experimental Study of Nanomagnets for Magnetic Quantumdot Cellular Automata (MQCA) Logic Applications.” University of Notre Dame (2005).

[29] S. Khizroev, Y. Hijazi, N. Amos, R. Chomko, and D. Litvinov. “Considerations in the Design of Three-Dimensional and Multi-Level Magnetic Recording.” J. Appl. Phys. **100**, 63907 (2006).

[30] S. Khizroev and D. Litvinov, “Perpendicular Magnetic Recording.” Kluwer Academic Publishers, (2005).

[31] Reiss, Günter, and D. Meyners. “Logic based on magnetic tunnel junctions.” Journal of Physics: Condensed Matter **19**.16: 165220 (2007).

[32] Wang, Jianguo, Hao Meng, and Jian-Ping Wang. “Programmable spintronics logic device based on a magnetic tunnel junction element.” Journal of applied physics **97**.10: 10D509-10D509 (2005).

[33] Lee, Seungyeon, et al. “Magneto-logic device based on a single-layer magnetic tunnel junction.” Electron Devices, IEEE Transactions on **54**.8: 2040-2044 (2007).

[34] Allwood, Dan A., et al. “Magnetic domain-wall logic.” Science **309**.5741: 1688-1692 (2005).

[35] Parkin, Stuart SP, Masamitsu Hayashi, and Luc Thomas. “Magnetic domain-wall racetrack memory.” Science **320**.5873: 190-194 (2008).

[36] Vernier, Nicolas, et al. “Domain wall propagation in magnetic nanowires by spin-polarized current injection.” EPL (Europhysics Letters) **65**.4: 526 (2004).

[37] Allwood, D. A., Gang Xiong, and R. P. Cowburn. “Writing and erasing data in magnetic domain wall logic systems.” Journal of applied physics **100**.12: 123908-123908 (2006).

[38] Yamanouchi, M., et al. “Current-induced domain-wall switching in a ferromagnetic semiconductor structure.” Nature **428**.6982: 539-542 (2004).

[39] L. D. Landau and E. M. Lifschitz. “On the theory of the dispersion of magnetic permeability in ferromagnetic bodies.” Phys. Z. Sowjet. **8**, 153 (1935).

[40] http://math.nist.gov/oommf/

[41] R. M. Bozorth, "Ferromagnetism." Piscataway, N.J., IEEE Press, (1993).

[42] N. Dao, S. L. Whittenburg and R. P. Cowburn. "Micromagnetics Simulation of Deep-submicron Supermalloy Disks." J. Appl. Phys. **90**, 5235 (2001).

[43] D. Litvinov, M. Kryder, and S. Khizroev. "Recording Physics of Perpendicular Media: Recording Layers." J. Magn. Magn. Mater. **241**, 453 (2002).

[44] P. C. Rickwood. "The Largest Crystals. American Mineralogist." **66**, 885 (1981).

[45] C. E., J. Rantschler, S. Khizroev, and D. Litvinov. "Micromagnetic Study of Domain Wall Dynamics in Bit-Patterned Nanodots." J. Appl. Phys. **103**, 113910 (2008).

[46] S. H. Charap, P.-L. Lu, and Y. He. "Thermal Stability of Recorded Information at High Densities." IEEE Trans. Magn. **33**, 978 (1997).

[47] C.E., J. Rantschler, S. Khizroev, and D. Litvinov. "Micromagnetics of Signal Propagation in Magnetic Cellular Logic Data Channels." J. Appl. Phys. **104**, 054311 (2008).

[48] Yuasa, Shinji, et al. "Giant room-temperature magnetoresistance in single-crystal Fe/MgO/Fe magnetic tunnel junctions." Nature materials **3**.12: 868-871 (2004).

[49] Park, B. G., et al. "A spin-valve-like magnetoresistance of an antiferromagnet-based tunnel junction." Nature materials **10**.5: 347-351 (2011).

[50] Barraud, C., et al. "Magnetoresistance in magnetic tunnel junctions grown on flexible organic substrates." Applied Physics Letters **96**.7: 072502-072502 (2010).

[51] M. Julliere. "Tunneling between ferromagnetic films." Phys. Lett. **54A**: 225–226. (1975).

[52] T. Miyazaki and N. Tezuka. "Giant magnetic tunneling effect in Fe/Al2O3/Fe junction "Giant magnetic tunneling effect in Fe/Al2O3/Fe junction." J. Magn. Magn. Mater. **139**: L231–L234 (1995).

[53] J. S. Moodera et al. "Large Magnetoresistance at Room Temperature in Ferromagnetic Thin Film Tunnel Junctions." Phys. Rev. Lett. **74** (16): 3273–3276 (1995).

[54] Tehrani, Said, et al. "Progress and outlook for MRAM technology." Magnetics, IEEE Transactions on **35**.5: 2814-2819 (1999).

[55] Gallagher, William J., and Stuart SP Parkin. “Development of the magnetic tunnel junction MRAM at IBM: From first junctions to a 16-Mb MRAM demonstrator chip.” IBM Journal of Research and Development **50**.1: 5-23 (2006).

[56] Nishimura, Naoki, et al. “Magnetic tunnel junction device with perpendicular magnetization films for high-density magnetic random access memory.” Journal of applied physics **91**.8: 5246-5249 (2002).

[57] Zhu, Xiaochun, and Jian-Gang Zhu. “Spin torque and field-driven perpendicular MRAM designs scalable to multi-Gb/chip capacity.” Magnetics, IEEE Transactions on **42**.10: 2739-2741 (2006).

[58] Kent, Andrew D. “Spintronics: Perpendicular all the way.” Nature Materials **9**.9: 699-700 (2010).

[59] Rossnagel, S. M., and J. Hopwood. “Metal ion deposition from ionized mangetron sputtering discharge.” Journal of Vacuum Science & Technology B: Microelectronics and Nanometer Structures **12**.1: 449-453 (1994).

[60] Chrisey, Douglas B., and Graham K. Hubler. “Pulsed laser deposition of thin films.” pp. 648. ISBN 0-471-59218-8. Wiley-VCH, (2003).

[61] Suzuki, Toshimasa, et al. “Nanosize-Controlled Syntheses of Indium Metal Particles and Hollow Indium Oxide Particles via the Sputter Deposition Technique in Ionic Liquids.” Chemistry of Materials **22**.18: 5209-5215 (2010).

[62] Chen, Wei, and Haroon Ahmed. “Fabrication of 5–7 nm wide etched lines in silicon using 100 keV electron-beam lithography and polymethylmethacrylate resist.” Applied physics letters **62**.13: 1499-1501 (1993).

[63] Vieu, C., et al. “Electron beam lithography: resolution limits and applications.” Applied Surface Science **164**.1: 111-117 (2000).

[64] Hicks, Erin M., et al. “Controlling plasmon line shapes through diffractive coupling in linear arrays of cylindrical nanoparticles fabricated by electron beam lithography.” Nano letters **5**.6: 1065-1070 (2005).

[65] Zeper, W. B., et al. “Perpendicular magnetic anisotropy and magneto-optical Kerr effect of vapor-deposited Co/Pt-layered structures.” Journal of Applied Physics **65**.12: 4971-4975 (1989).

[66] Qiu, Z. Q., and S. D. Bader. "Surface magneto-optic Kerr effect." Review of Scientific Instruments **71**.3: 1243-1255 (2000).

[67] Tse, Wang-Kong, and A. H. MacDonald. "Giant magneto-optical Kerr effect and universal Faraday effect in thin-film topological insulators." Physical review letters **105**.5: 057401 (2010).

[68] Gewirth, Andrew A., and Brian K. Niece. "Electrochemical applications of in situ scanning probe microscopy." Chemical reviews **97**.4: 1129-1162 (1997).

[69] Salapaka, Srinivasa M., and Murti V. Salapaka. "Scanning probe microscopy." Control Systems, IEEE **28**.2: 65-83 (2008).

[70] Martin, Y., and H. Kumar Wickramasinghe. "Magnetic imaging by force microscopy with 1000 Å resolution." Applied Physics Letters **50.**20: 1455-1457 (1987).

[71] Mamin, H. J., et al. "Magnetic force microscopy of thin Permalloy films." Applied physics letters **55**.3: 318-320 (1989).

[72] Puntes, Victor F., et al. "Collective behaviour in two-dimensional cobalt nanoparticle assemblies observed by magnetic force microscopy." Nature materials **3**.4: 263-268 (2004).

[73] Dieter W, Mary FD. "Extremely high-density longitudinal magnetic recording media." Annu. Rev. Mater. Sci. **30**: 611–44 (2000).

[74] Gerardo AB, Sudhir M, Bo B, Jackie T, Michael A, et al. "Longitudinal Magnetic Media Designs for 60–200 Gb/in^2 "Recording. IEEE Trans. Mag., **39** (2): 651–656 (2003).

[75] Piramanayagam SN. "Perpendicular recording media for hard disk drives." J. Appl. Phys. **102**: 011301 (2007).

[76] William AC, Chubing P, Amit VI, Darren K, Wei P, et al. "Heat-assisted magnetic recording by a near-field transducer with efficient optical energy transfer." Nature Photonics **3**: 220–224 (2009).

[77] Michael AS, William AC, Edward G, Nils G, Ganping J, et al. "Integrated Heat Assisted Magnetic Recording Head: Design and Recording Demonstration." IEEE Trans. Mag. **44** (1): 119–124 (2008).

[78] Nils JG, Hua Z, Darren K, Sharat B, Mike M. "Effect of gradient alignment in heat assisted magnetic recording." J. Appl. Phys.**105**: 07B905 (2009).

[79] Zhang L, Takahashi YK, Perumal A, Hono K. “L10-ordered high coercivity (FePt) Ag–C granular thin films for perpendicular recording.” J. Magn. Mag. Mat. **322**: 2658–2664 (2010).

[80] Amos, N., Butler, J., Lee, B., Shachar, M. H., Hu, B., Tian, Y., & Khizroev, S. “Multilevel-3D Bit Patterned Magnetic Media with 8 Signal Levels Per Nanocolumn.” PloS one, **7**(7), e40134 (2012).

[81] Manfred A, Olav H, Guohan H, Bruce DT. “Method for magnetic recording on patterned multilevel perpendicular media using thermal assistance and fixed write current.” US Patent 6865044 (2005).

[82] Alexander YD, Hans JR, Erol G. “Single-Pass Recording of Multilevel Patterned Media.” US Patent 7974031 (2010).

[83] Mehmet FE, Mourad B, Walter RE. “Multi-level recording on shingled coherent magnetic media.” US Patent 7982994 (2011).

[84] Shah P, Ahmed M, Ambroze M, Tjhai C, Davey PJ “Novel Soft-Feedback Equalization Method for Multilevel Magnetic Recording.” IEEE Trans. Mag. **43**(6): 2280– 282 (2007).

[85] Baltz V, Landis S, Rodmacq B, Dieny B. “Multilevel magnetic media in continuous and patterned films with out-of-plane magnetization.” J. Magn. Mag. Mat. **290–291**: 1286–1289 (2005).

[86] Albrecht M, Hu G, Moser A, Hellwig O, Terris BD. “Magnetic dot arrays with multiple storage layers.” J. Appl. Phys. **97**: 103910 (2005).

[87] Y. Tian, N. Amos, B. Hu, D. Litvinov, and S. Khizroev, “Considerations in the design of a highly scalable magnetic logic channel.” BP-12, The 55th Magnetism and Magnetic Materials (MMM) Conference, Atlanta, Georgia, November (2010).

[88] Tsoi M, Jansen AGM, Bass J, Chiang WC, Seck M, Tsoi V, Wyder P. “Excitation of a magnetic multilayer by an electric current.” Phys. Rev Lett. **80**:4281–4284 (1998).

[89] J. C. Slonczewski, “Currents and torques in metallic magnetic multilayers.” J. Magn Magn Mater **247**:324–329 (2002).

[90] L. Berger, “Emission of spin waves by a magnetic multilayer traversed by a current.” Phys Rev B **54**:9353–9358 (1996).

[91] Ralph, D. C., & Stiles, M. D, "Spin transfer torques." Journal of Magnetism and Magnetic Materials, **320**(7), 1190-1216 (2008).

[92] S. Ikeda, K. Miura, H. Yamamoto, K. Mizunuma, H. D. Gan, M. Endo, S. Kanai, J. Hayakawa, F. Matsukura, and H. Ohno, "A perpendicular-anisotropy CoFeB–MgO magnetic tunnel junction." Nat. Mater. **9**, 721 (2010).

[93] M. Gajek, J. J. Nowak, J. Z. Sun, P. L. Trouilloud, E. J. O'Sullivan, D. W. Abraham, M. C. Gaidis, G. Hu, S. Brown, Y. Zhu, R. P. Robertazzi, W. J. Gallagher, and D. C. Worledge, "Spin torque switching of 20 nm magnetic tunnel junctions with perpendicular anisotropy." Appl. Phys. Lett. **100**, 132408 (2012).

[94] R. Sbiaa, S. Y. H. Lua, R. Law, H. Meng, R. Lye, and H. K. Tan, J. "Reduction of switching current by spin transfer effect in perpendicular anisotropy magnetoresistive devices." Appl. Phys. **109**, 07C707 (2011).

[95] Hong, Jeongmin, P. Liang, V. L. Safonov, S. Khizroev, "Energy-efficient spin-transfer torque magnetization reversal in sub-10-nm magnetic tunneling junction point contacts." Journal of Nanoparticle Research **15**.4, 1-6 (2013).

[96] S. Mukherjee, D. Litvinov, and S. Khizroev, "Atomic-scale modeling of nanoconstrictions." IEEE Trans. Magn. **40** (4), 2143-5 (2004).

[97] S. Ikeda, J. Hayakawa, Y. Ashizawa, Y.M. Lee, K. Miura, H. Hasegawa, M. Tsunoda, F. Matsukura and H. Ohno. "Tunnel magnetoresistance of 604% at 300 K by suppression of Ta diffusion in CoFeB/MgO/CoFeB pseudo-spin-valves annealed at high temperature." Appl. Phys. Lett. **93** (8): 082508 (2008).

[98] Slonczewski, J. C. "Theory of domain-wall motion in magnetic films and platelets." Journal of Applied Physics **44**.4: 1759-1770 (1973).